Simulated ENSO in a Global Coupled Ocean–Atmosphere Model: Multidecadal Amplitude Modulation and CO_2 Sensitivity

THOMAS R. KNUTSON AND SYUKURO MANABE

Geophysical Fluid Dynamics Laboratory/NOAA, Princeton, New Jersey

DAIFANG GU

Program in Atmospheric and Oceanic Sciences, Princeton University, Princeton, New Jersey

(Manuscript received 25 October 1995, in final form 24 June 1996)

ABSTRACT

An analysis is presented of simulated ENSO phenomena occurring in three 1000-yr experiments with a low-resolution (R15) global coupled ocean–atmosphere GCM. Although the model ENSO is much weaker than the observed one, the model ENSO's life cycle is qualitatively similar to the ''delayed oscillator'' ENSO life cycle simulated using much higher resolution ocean models. Thus, the R15 coupled model appears to capture the essential physical mechanism of ENSO despite its coarse ocean model resolution. Several observational studies have shown that the amplitude of ENSO has varied substantially between different multidecadal periods during the past century. A wavelet analysis of a multicentury record of eastern tropical Pacific SST inferred from $\delta^{18}O$ measurements suggests that a similar multidecadal amplitude modulation of ENSO has occurred for at least the past three centuries. A similar multidecadal amplitude modulation occurs for the model ENSO (2–7-yr band), which suggests that much of the past amplitude modulation of the observed ENSO could be attributable to internal variability of the coupled ocean–atmosphere system. In two 1000-yr CO_2 sensitivity experiments, the amplitude of the model ENSO decreases slightly relative to the control run in response to either a doubling or quadrupling of CO_2. This decreased variability is due in part to CO_2-induced changes in the model's time-mean basic state, including a reduced time-mean zonal SST gradient. In contrast to the weaker overall amplitude, the multidecadal amplitude *modulations* become more pronounced with increased CO_2. The frequency of ENSO in the model does not appear to be strongly influenced by increased CO_2. Since the multidecadal fluctuations in the model ENSO's amplitude are comparable in magnitude to the reduction in variability due to a quadrupling of CO_2, the results suggest that the impact of increased CO_2 on ENSO is unlikely to be clearly distinguishable from the climate system ''noise'' in the near future—unless ENSO is substantially more sensitive to increased CO_2 than indicated in the present study.

1. Introduction

An intriguing feature of El Niño/Southern Oscillation (ENSO) has been its substantial variation in amplitude during the past century. Analysis of historical observations of SST indicate that El Niño had relatively high amplitude during the period 1885–1915, followed by a few decades of relatively low amplitude (1915–1950), followed by a return to higher amplitudes since about 1960 (Gu and Philander 1995; Wang and Ropelewski 1995; Rasmusson 1993, personal communication). Trenberth and Shea (1987) found evidence for similar multidecadal fluctuations in the prominence of the Southern Oscillation, based on historical sea level pressure observations. These multidecadal changes in ENSO are clearly evident in a time series of observed SST (2–7 yr filtered) for the NINO3 region (Fig. 1b), based on COADS data (Pan and Oort 1990). Similarly, a four century time series of normalized NINO3 region SST from our coupled GCM (Fig. 1a) shows substantial fluctuations in amplitude on a multidecadal timescale. In this report, these multidecadal-scale fluctuations in ENSO amplitude are investigated, including their implication for climate change detection. Several investigators have begun using historical and paleoclimatic proxy records extending back beyond the past century to search for variations in both the frequency (or return interval) and amplitude of ENSO on multidecadal to century timescales (e.g., Michaelsen 1989; Enfield and Cid S. 1991; Diaz and Markgraf 1992; Dunbar et al. 1994; Diaz and Pulwarty 1994). In the present study, the paleo-SST record of Dunbar et al. (1994) is used to provide a longer-term perspective on ENSO's modulation behavior in comparison to our model.

Given that the amplitude of ENSO—and possibly its frequency—have varied substantially in the past for still

Corresponding author address: Thomas R. Knutson, NOAA/GDFL, P.O. Box 308, Princeton, NJ 08542.
E-mail: tk@gfdl.gov

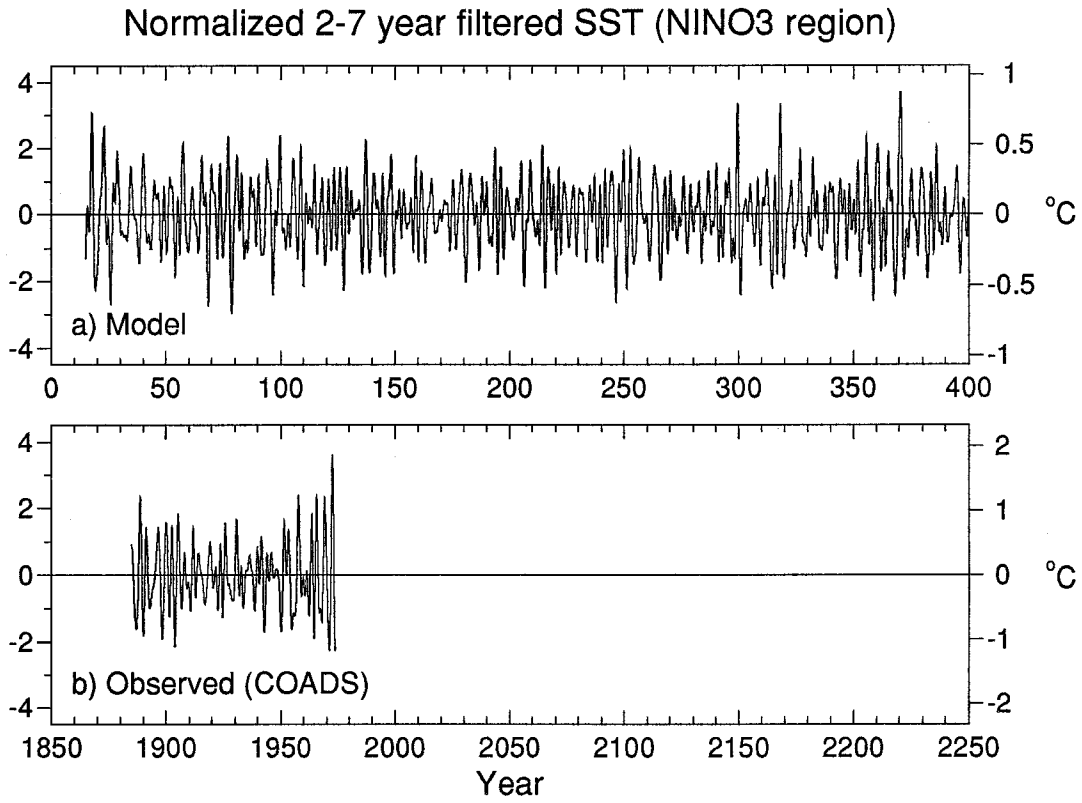

FIG. 1. Normalized timeseries of 2–7 yr filtered SST anomalies for the region 4°N–4°S, 150°–90°W (which is approximately the ''NINO3 region'') based on (a) R15 coupled GCM control run, years 1–400; or (b) observed SSTs from COADS (Pan and Oort 1990). The data were normalized by dividing by the standard deviation. The temperature anomaly scale (°C) appropriate to each time series is shown on the right-hand side of each diagram.

undetermined reasons, it is important to begin to examine whether a CO_2-induced global warming could have an important impact on ENSO. As a further motivation, Zebiak and Cane (1987, 1991) have found that the amplitude and frequency of their model's ENSO can be altered by changing parameters affecting the strength of atmosphere–ocean coupling. One can speculate that during ENSO episodes in a CO_2-warmed climate, the much larger atmospheric moisture content and evaporation rates would allow for enhanced moisture convergence and condensational heating anomalies over the tropical Pacific, which could act to strengthen the atmospheric component of the oscillation.

Therefore, concerning the relationship of ENSO to CO_2-induced global warming, the following questions can be posed:

1) Could a CO_2-induced global warming lead to an increase in the amplitude of ENSO?
2) How would the frequency of ENSO change with increased CO_2?
3) Could the climate enter a ''permanent El Niño'' state due to increased CO_2?
4) How does the ''natural variability'' of ENSO's amplitude compare to the impact of increased CO_2?

These questions (particularly 1, 2, and 4) are addressed in this report, using three 1000-yr simulations of a global coupled ocean–atmosphere general circulation model (GCM). Concerning question 3 (the possibility of a ''permanent El Niño'' state), Knutson and Manabe (1995) did not find evidence for such a response in their coupled GCM, even with a quadrupling of CO_2. Rather, a quadrupling of CO_2 in their model produced a ~1°C reduction in the east–west SST contrast in the tropical Pacific as compared with a much larger (4°–5°C) overall warming of the region. ENSO-like fluctuations continued to occur about the modified mean state, although they were slightly weaker in the warmer climate (Knutson and Manabe 1994).

Since the preliminary study of ENSO's response to increased CO_2 (Knutson and Manabe 1994), further analysis has revealed that our model's ENSO is qualitatively more realistic than has been recognized previously. This result, presented in section 3, is important because it implies that the model contains the essential physical mechanism of ENSO despite the coarse resolution required for multicentury integrations. (The term ''model ENSO'' is used when discussing the ENSO-like phenomenon in the model, recognizing that while the model's phenomenon has deficiencies as a simulation of ENSO, it also has a considerable degree of realism,

as discussed in this report.) In section 4, wavelet analysis (Gu and Philander 1995) is used to document a substantial modulation of ENSO's amplitude on a multidecadal timescale, both in the model and observations, with the latter inferred from a multicentury $\delta^{18}O$ proxy record of eastern equatorial Pacific SST (Dunbar et al. 1994). In section 5, the sensitivity of the model ENSO to increased CO_2 is examined primarily using spectral analysis and running standard deviation plots. The wavelet and running standard deviation techniques play complementary roles in the analysis. For instance, the wavelet technique is particularly well-suited for resolving the amplitude modulation behavior on a variety of different timescales, since its window width varies as a function of the timescale. On the other hand, the running standard deviation technique is particularly useful for smoothing out the multidecadal amplitude modulation ''noise'' to reveal the multicentury-scale CO_2-induced ''signal,'' since a much wider window can be used (compared to the wavelet technique) for a comparable loss of data due to end effects. In Knutson and Manabe (1994), only the running standard deviation technique (with a 100-yr window) was used, since the focus there was specifically on the longer timescale (e.g., CO_2-induced) changes in ENSO. However, as a result, the multidecadal amplitude modulation behavior of the model was not clearly apparent, as it is in the present study.

Three 1000-yr experiments are available for analysis in the present study. The availability of such long coupled GCM simulations is a unique aspect of the analysis, which provides two important advantages: (i) the internally generated multidecadal amplitude modulations of the model's ENSO are well-sampled and can thus be meaningfully compared with ENSO's amplitude variability as inferred from historical observations or paleoclimate proxy records; and (ii) the long simulation allows a modest CO_2-induced signal to be identified in the model despite the presence of substantial ''noise'' resulting from the multidecadal amplitude modulation. In contrast, previous analyses of the impact of increased CO_2 on ENSO using coarse-resolution coupled climate models have relied on much shorter simulations. For example, Meehl et al. (1993) compared results obtained from a 15-yr integration period with doubled CO_2 and a simulation with the normal CO_2 concentration ($1 \times CO_2$), whereas Tett compared results from two 75-yr simulations during which CO_2 was either increasing at 1% per year (compounded) or constant at $1 \times CO_2$. Thus, the 1000-yr coupled model simulations provide a unique perspective on both the CO_2–ENSO sensitivity issue and on the multidecadal to century timescale variations of ENSO frequency and amplitude inferred from historical and paleoclimate records.

2. Description of model, experiments, and data preparation

The coupled ocean–atmosphere model and experimental design used here are described in Manabe and Stouffer (1994), and references therein. Briefly, the atmospheric component is a global nine-level GCM, with horizontal distributions of variables represented in both spectral (rhomboidal truncation at zonal wavenumber 15) and gridpoint (7.5° long. by 4.5° lat. computational grid) domains. The ocean component is a global 12-level gridpoint GCM with 3.75° long. by 4.5° lat. resolution and a 50-m thick top layer. The model has interactive clouds and seasonally varying solar insolation.

The initial condition for the time integration of the coupled model has realistic seasonal and geographical distributions of surface temperature, surface salinity, and sea ice, with which both the atmospheric and oceanic model states are nearly in equilibrium. When the time integration of the coupled model starts from this initial condition, the model drifts toward its own equilibrium state, which differs from the initial condition described above. To reduce this drift from a realistic initial condition, the interfacial fluxes of heat and water obtained from the atmospheric component of the coupled model are modified by given amounts before these are imposed upon the ocean surface (Manabe et al. 1991). Since the flux adjustments are determined prior to the time integration of the coupled model and are not correlated to the transient surface anomalies of temperature and salinity, in a linear sense they are unlikely to either systematically amplify or damp the anomalies. [Lau et al. (1992) found ENSO-like fluctuations similar to those described here using a similar model but with no heat flux adjustment, indicating that the model's ENSO appears in the absence of heat flux adjustment.] Obviously, these flux adjustments do not eliminate the shortcomings of the model physics, including the effect of these deficiencies on the simulated ENSO. However, the adjustments do prevent the rapid drift of the simulated state from the realistic initial condition, which otherwise could seriously distort the results of a numerical experiment. For example, if tropical SSTs were allowed to drift by several degrees from the observed initial condition, the evaporative damping of SST anomalies during model ENSO events would be substantially changed, possibly distorting the model's ENSO phenomenon.

Three 1000-yr experiments from this model serve as the primary source of model data for this analysis. The control experiment has constant CO_2 throughout. In the $4 \times CO_2$ experiment, CO_2 increases at 1% yr^{-1} compounded until it quadruples (140 years), then remains fixed at four times the initial level for the remaining 860 years. In the $2 \times CO_2$ experiment, the CO_2 concentration increases at 1% yr^{-1} compounded to $2 \times CO_2$ over 70 years, then remains fixed at twice its initial level for the remaining 930 yr. Due to resource constraints, some of the analyses (particularly those requiring many model variables) are limited to 200-yr integration segments, rather than the full 1000 yr. However, for examinations of CO_2-induced changes in variability or multidecadal amplitude modulations (where signal-to-

noise issues are of greatest concern), model datasets of 820 to 1000 yr in length are used.

The model data for the regression and CO_2 sensitivity analyses in sections 3 and 5 were bandpass-filtered using filters designed following Hamming (1977, chapter 7). Except as noted, results are based on a 2–7 yr bandpass filter with response >0.5 at periods from 21 to 89 months and >0.9 from 22 to 75 months. A second period range (8–15 yr) was examined separately for some analyses. For the 8–15 yr filter, the response was >0.5 at periods from 90 to 210 months and >0.9 from 110 to 150 months. In Knutson and Manabe (1994), the 2–15 yr band was analyzed, effectively combining the two bands considered separately in this analysis. The rationale for examining the 2–7 and 8–15 yr ranges separately will be discussed in section 4. In the present study, some calculations using a high-pass (<21 mo) filter are also referred to; in this case the mean seasonal cycle was removed from the data before filtering.

The primary multicentury observational record of ENSO used in this study is the Galápagos coral $\delta^{18}O$ record of Dunbar et al. (1994). This dataset is believed to be a useful proxy record of annual mean eastern Pacific SST over the past 350+ years. It is particularly useful for this study given that changes in the amplitude and frequency of ENSO on multidecadal to multicentury timescales are to be examined. Thirteen missing points in the annual-resolution $\delta^{18}O$ record were filled by linear interpolation, including an eight-year section from 1954 to 1961. Data after 1961 (UR-87) were adjusted by adding 0.4‰ following Dunbar et al. Although only the Galápagos coral record is used in the present analysis, other long-term ENSO-sensitive climate indices are also available (Diaz and Pulwarty 1994) and could be incorporated in a future study.

3. Description of the model's ENSO

a. Life cycle description

An important step in a model-based investigation of ENSO is an evaluation of the model's ability to simulate various observed aspects of ENSO. The SST fluctuations for the model's ENSO are much weaker than those observed. For example, the standard deviation of 2–7-yr filtered SST for the NINO3 region (Fig. 1) is 0.24°C for the model, or 46% of the observed value (0.52°C) based on COADS data (Pan and Oort 1990) for the past century. The failure to simulate a realistic ENSO amplitude is a problem common to several other coarse-grid coupled GCMs (Meehl 1990; Lau et al. 1992; Meehl et al. 1993; Tett 1995; Neelin et al. 1992). Nonetheless, in this section the life cycle of the model's ENSO is examined in order to assess whether at least the essential physical mechanism of ENSO is captured in the model.

Life cycles of the model ENSO are constructed using lagged linear regression analysis of 2–7 yr bandpass-filtered data from years 1–200 of the control experiment. The reference SST index for the regression analysis is an area-average of SST over the region 7°N–7°S, 173°E–120°W, which is the area of maximum interannual SST variability in the model's equatorial Pacific. The ocean heat content anomalies discussed in this section are defined as the vertically integrated temperature anomaly over depths of 51 to 595 m. The heat content is integrated over a deeper layer of the ocean than in some previous modeling studies (e.g., Philander et al. 1992) since the thermocline is more diffuse in the tropical Pacific of our model than in the real world or in higher resolution ocean models. The top model layer is not included in the vertically integrated heat content anomalies, since it is examined separately (i.e., the SST life cycle). The term ''heat content propagation'' is used to describe the apparent movement (or phase propagation) of heat content anomalies over time.

Figure 2 shows the regression of subsurface ocean heat content anomalies versus the SST index for lags of -24 months to $+24$ months at three-month intervals. Figures 3 and 4 show the corresponding regression results for SST and equatorial ocean temperature as a function of depth, respectively. The sequence of maps in Figs. 2–4 represents a ''life cycle'' of the model ENSO in the sense that it depicts the time evolution of various model fields for a ''composite'' model event. The oceanic component of the life cycle is emphasized here (Figs. 2–4). A subset of the atmospheric component of the life cycle (surface winds, precipitation, and heat balance) will be discussed in section 5, and a map of the correlation between sea level pressure and the SST index (>2 yr filtered model data) is shown in Knutson and Manabe (1994).

The life cycle (Figs. 2–4) begins arbitrarily at a time of relatively cool (La Niña) SST conditions in the central equatorial Pacific (Fig. 3a; lag -24 months) with two positive heat content (depressed thermocline) anomalies centered off-equator (16°N and 10°S) in the western tropical Pacific (Fig. 2a). In the extreme eastern Pacific is a region of negative heat content anomalies centered on the equator (Fig. 2a). The region of positive heat content anomalies in the west expands eastward along the equator (Figs. 2b–e; lags -21 to -12 months), as the region of negative heat content anomalies in the eastern Pacific splits into two separate regions straddling the equator. At lag -9 to -3 months (Figs. 2f–h), positive heat content anomalies become well-established throughout the central to eastern equatorial Pacific, now accompanied by substantial positive SST anomalies in the central Pacific sector (Figs. 3g–h). The SST regression pattern at this stage resembles Rasmusson and Carpenter's (1982) Mature Phase composite. However, the relatively small SST anomalies in the extreme eastern Pacific during the model's SST lifecycle indicate that the model ENSO's SST variability is too small in the eastern Pacific compared with typical (though not all) observed events (Rasmusson and Carpenter 1982).

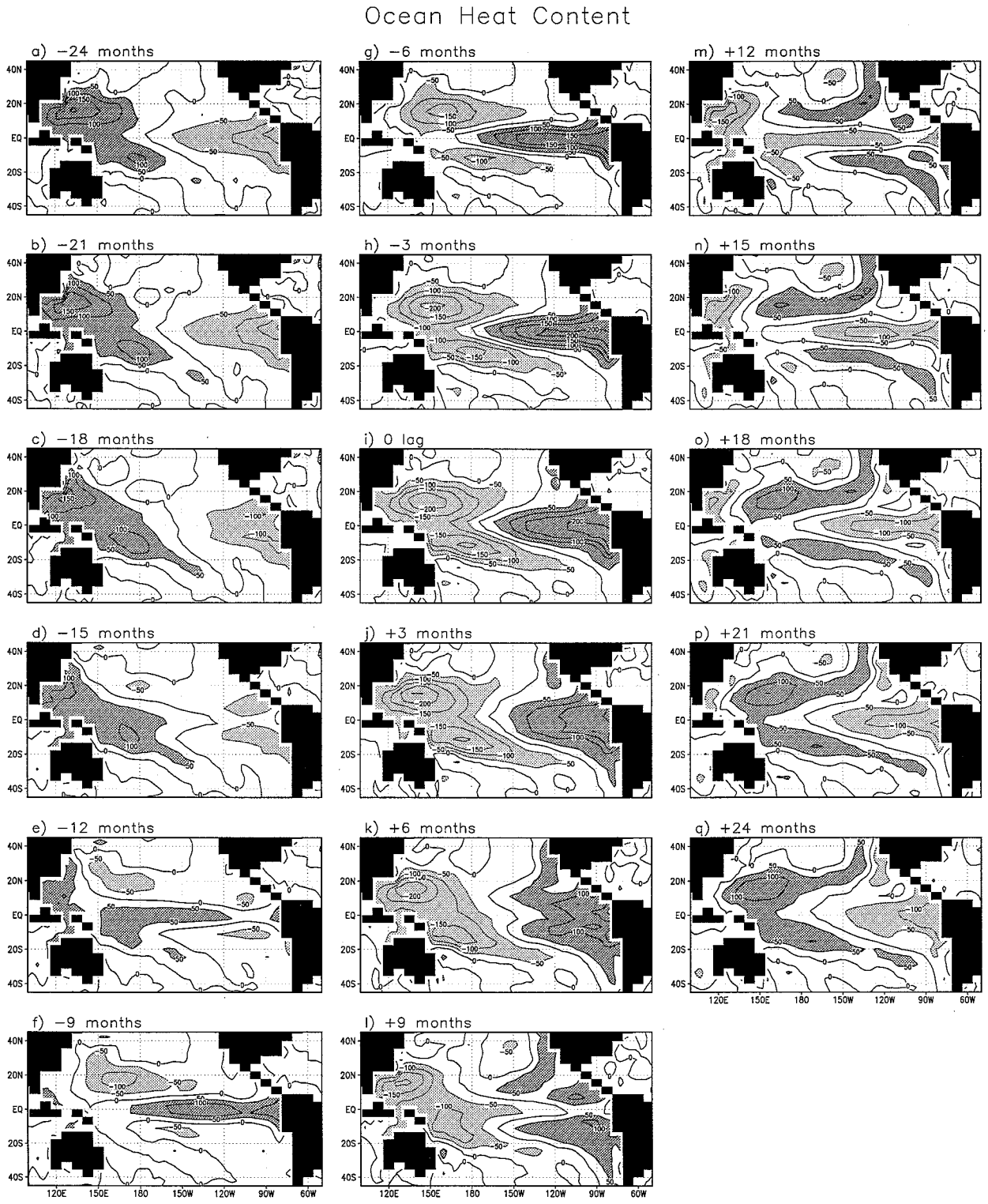

FIG. 2. Heat content anomaly life cycle, based on lagged regression of 51–595-m vertically integrated heat content anomalies vs SST (averaged 7°N–7°S, 172.5°E–120°W). Data are 2–7-yr bandpass-filtered time series from years 16–185 of the control run. Contour interval: 50 m; values greater than 50 m or less than −50 m have dark and light shading, respectively. The lag in months for each panel is displayed above the appropriate panel.

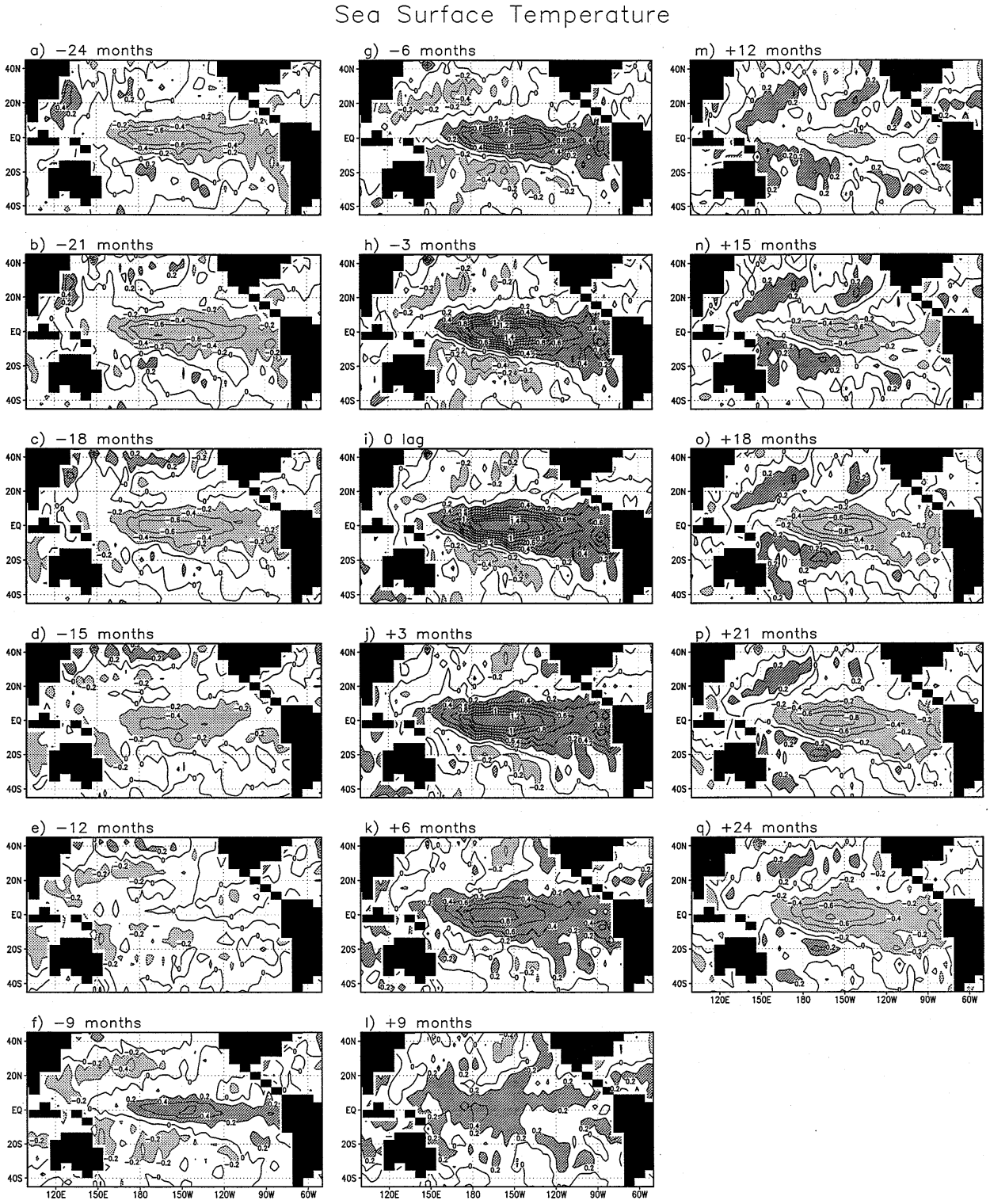

FIG. 3. As in Fig. 2 but for SST at all points vs SST (7°N–7°S, 173°E–120°W). Contour interval: 0.2 (dimensionless); values greater than 0.2 or less than −0.2 have dark and light shading, respectively.

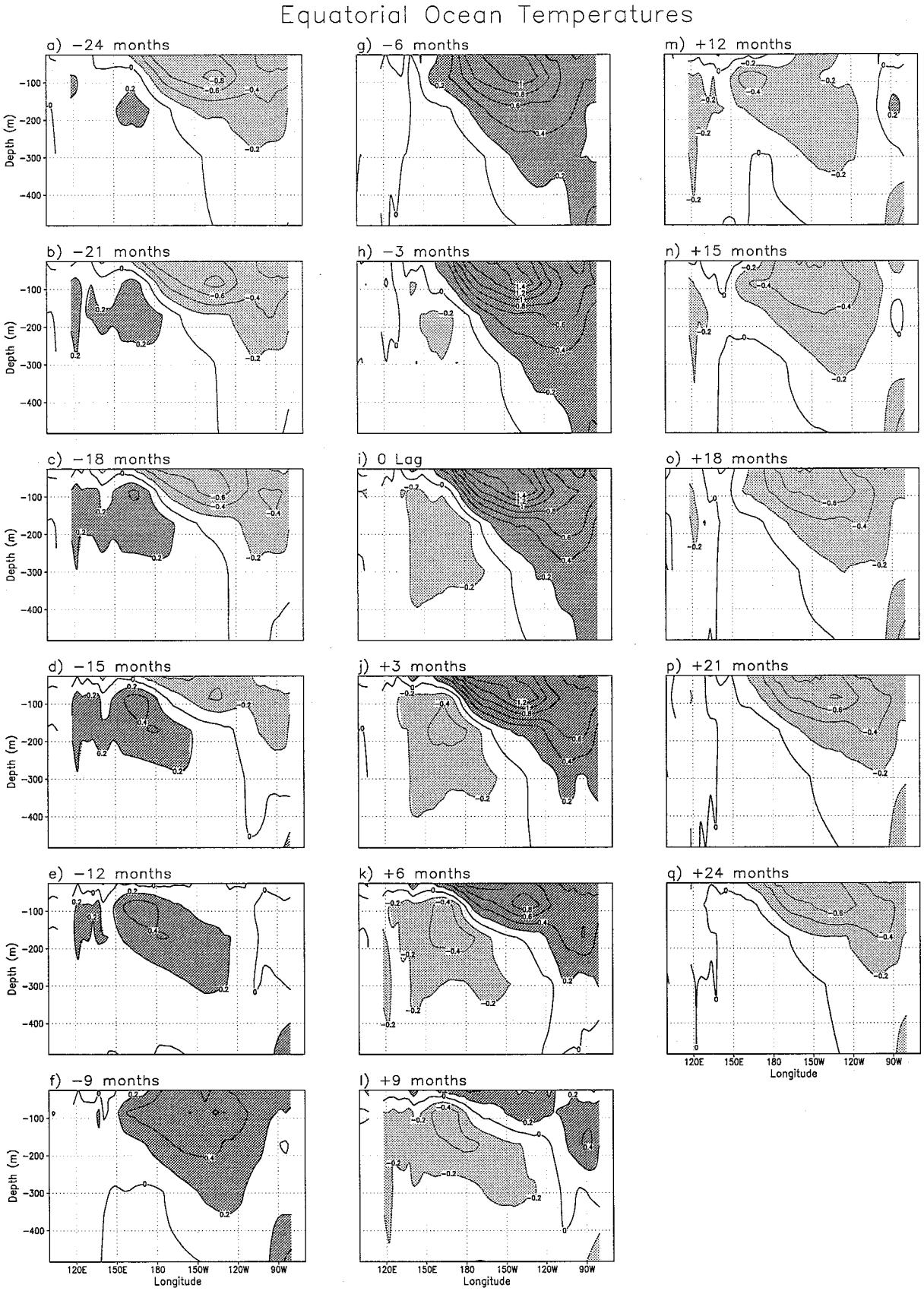
Equatorial Ocean Temperatures
a) −24 months
b) −21 months
c) −18 months
d) −15 months
e) −12 months
f) −9 months
g) −6 months
h) −3 months
i) 0 Lag
j) +3 months
k) +6 months
l) +9 months
m) +12 months
n) +15 months
o) +18 months
p) +21 months
q) +24 months
Depth (m)
−100
−200
−300
−400
120E
150E
180
150W
120W
90W
Longitude

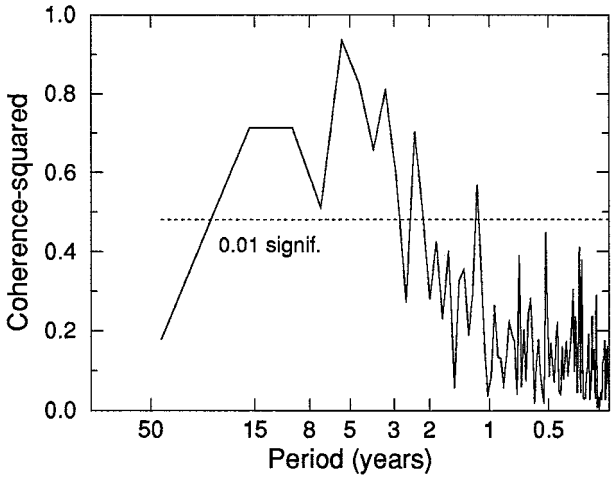

FIG. 5. Coherence-squared spectrum for SST (7°N–7°S, 173°E–120°W) vs ocean heat content (11°S, 174°E; 51–595-m vertically integrated) for years 1–200 of the control experiment. Each estimate plotted is based on a sum of eight adjacent calculable frequencies (nonoverlapping rectangular window). The time series were prefiltered by removing the mean seasonal cycle and linear trend. Points lying above the dashed line are significantly different from zero at the 0.01 significance level.

Coupled model ENSO simulations using a much higher resolution ocean model (Philander et al. 1992) also show much higher SST variability in the eastern Pacific than occurs in our model. The substantial warm SST anomalies at lag −12 to −6 months (Figs. 2e–g) are associated with a pattern of wind stress curl (not shown) which begins, via Ekman pumping, to cause an elevation of the thermocline off-equator in the western Pacific (Figs. 3e–g). This sets the stage for the later onset of a ''cold event,'' which will eventually terminate the warm event in progress (see also Chao and Philander 1993). Meanwhile, the event reaches its peak warming phase (lags −3 to +3 months), with pronounced SST anomalies and strong east–west contrast in heat content anomalies (Figs. 2, 3h–j). In the termination phase (Figs. 2, 3k–n; lags +6 to +15 months), the negative heat content anomalies in the west propagate eastward along the equator to the eastern Pacific, and the warm SST anomalies are replaced by cool anomalies along the equator. The heat content anomaly patterns during the life cycle are qualitatively similar to those obtained in an ENSO simulation using a much higher-resolution ocean model forced by observed winds (Chao and Philander 1993; Fig. 8).

Figure 4 shows the evolution of ocean temperature regression anomalies along the equator as a function of depth. The results show that substantial ocean temperature anomalies are not limited to the top (50 m) model ocean layer, but extend downward a few hundred meters into the ocean. The warm SST anomalies in the central Pacific at lag −9 months (Fig. 4f, Fig. 3f) appear to originate from *subsurface* warm anomalies in the western equatorial Pacific (Figs. 4a–e; lags −24 to −12 months), which appear to propagate upward and eastward to meet the surface by lag −9 months (Fig. 4f). This feature of the model ENSO life cycle is consistent with an analysis of ocean perturbations during El Niño/La Niña obtained using a much higher resolution ocean model forced with observed winds (Goddard 1995). After becoming established at the surface, the temperature (i.e., SST) anomalies intensify but remain almost stationary with only a slight westward propagation evident at the surface (Figs. 4f–k; Figs. 3f–k; lags −9 to +6 months). Thus, although the model's ENSO appears to be almost a standing oscillation when viewed in terms of the SST anomalies (Fig. 3), in fact the *subsurface* temperature perturbations (i.e., thermocline perturbations) display extensive propagation around the tropical Pacific basin during the life cycle (Figs. 2, 4), a feature that will be discussed further later in this section. It is this ocean subsurface evolution that provides the ''memory'' in the system for the model's ENSO (e.g., Chao and Philander 1993). In the central equatorial Pacific, where the subsurface perturbations become exposed at the surface, the quasi-stationary SST signature of the model's ENSO is seen.

b. Coherence between surface and subsurface temperature fluctuations

In this section cross-spectral analysis is used to assess the statistical significance of the association between SST and the subsurface temperature perturbations in the model, and to estimate timescales over which the relationship is most coherent. The resulting coherence spectrum between time series of central equatorial Pacific SST and western tropical Pacific subsurface heat content in the model is shown in Fig. 5. The results shown are based on a 200-yr segment of the R15 control run, using the SST for the region 7°N–7°S, 173°E–120°W versus ocean heat content (51 to 595 m) for the region 11°S, 174°E. (Similar results are obtained using ocean heat content series from other locations in the western Pacific.) The statistical significance is assessed according to the procedure of Julian (1975). The coherence spectrum indicates that SST and subsurface heat content are significantly correlated on timescales of about 3 to 15 yr, with a maximum coherence between 5 and 6 yr. At periods of two years and less, the coherence generally does not exceed the 0.01 significance level except for a few isolated peaks (e.g., near 14

←

FIG. 4. As in Fig. 2 but for ocean temperature (averaged 2°N–2°S) as a function of depth (meters) and longitude vs SST (7°N–7°S, 173°E–120°W). Contour interval: 0.2 (dimensionless); values greater than 0.2 or less than −0.2 have dark and light shading, respectively.

months). For the life cycle, the focus is on the 2–7-yr band rather than the 2–15-yr band (despite the high coherence for periods up to 15 yr) for reasons which will be elaborated in section 4. However, the anomaly patterns in the life cycle obtained using 8–15-yr filtered data are similar to those shown in Figs. 2–4, except the anomalies have a slightly greater meridional extent, and the time lag between different stages of the life cycle is longer (i.e., the phase propagation is slower).

c. Subsurface evolution during individual events

The evolution of heat content anomalies for *individual model ENSO events* during a period of the control integration is depicted in time-longitude format in Fig. 6. Anomalies are shown for both the equator (middle panel) and 11°S (repeated on the left and right panels). Similar results are obtained using 11°N rather than 11°S. For this diagram, longitudes have been reversed on the two (identical) 11°S panels so that a signal that propagates eastward along the equator then back westward at 11°S will appear as a continuous strip running from upper left to lower right on the diagram. In several events in Fig. 6, a signal can be traced through such a complete circuit of the basin (e.g., years 70–80). Thus, in some cases in the model, the off-equatorial anomalies in the western basin appear to be linked to a propagating feature coming from the eastern boundary of the basin. However, in other cases the westward propagating feature at 11°S can be quite indistinct in the eastern part of the basin (e.g., years 110–120), or the equatorial feature is difficult to trace back to an earlier westward propagating anomaly (e.g., year 120).

The heat content evolution in Fig. 6 can be compared with the ''delayed oscillator'' life cycle as described by Schopf and Suarez (1988) or with a coupled model simulation of ENSO using a model very similar to ours but with a much higher-resolution ocean component (Philander et al. 1992; see also Chao and Philander 1993). Eastward phase propagation along the equator is a feature of Fig. 6 also seen in these higher-resolution ENSO models. In all the models there is evidence for strong off-equatorial thermocline perturbations in the western tropical Pacific. There is some evidence for off-equatorial westward phase propagation in all the models, although there are differences among them in the details of this feature. For example, Schopf and Suarez note that in their model, substantial westward propagating signals originate not at the eastern boundary of the ocean basin but from the *central* part of the basin (via wind stress anomalies), a process which they termed ''coupled reflection.'' Philander et al. (1992) found pronounced off-equatorial westward phase propagation of heat content in the *eastern* Pacific, but these features did not appear to propagate across the entire basin. In our model, off-equatorial thermocline perturbations propagate westward across the basin, but only for some of the events. Whether this feature of our model is important to the simulated ENSO remains to be seen. It may represent occasional phase-locking of a westward propagating feature with an otherwise ongoing model ENSO event. We conclude that while there are some differences in detail between the models, the evolution of thermocline perturbations during our model's ENSO is qualitatively similar to that obtained using much higher-resolution ENSO models.

d. Interpretation of the model's ENSO phenomenon

Based on model results shown in Figs. 2–6, we interpret the model's ENSO as probably more closely related to the ''delayed oscillator'' mechanism (e.g., Schopf and Suarez 1988; Graham and White 1988; Battisti and Hirst 1989) than to the westward propagating ''SST mode'' of Neelin (1991). This assessment is based on the following characteristics of the model ENSO: (i) the systematic basin-wide propagation of subsurface heat content anomalies (Figs. 2, 4, 6); (ii) the very limited phase propagation of SST anomalies (Figs. 3, 4); and (iii) the strong statistical association between the propagating subsurface temperature anomalies and the quasi-stationary SST anomalies (Figs. 2–5). The strong association between subsurface and surface anomalies during the model ENSO indicates that subsurface ocean dynamics (i.e., subsurface ocean ''memory'') plays an important role in our coupled model's phenomenon, as it apparently does for the real ENSO (Chao and Philander 1993).

The interpretation of the model's ENSO in terms of the ''delayed oscillator'' mechanism differs from earlier assessments (e.g., Neelin 1991; Chao and Philander 1993) in which it has been suggested that the GFDL R15 model phenomenon can be interpreted as an SST mode. [In a subsequent study, Jin and Neelin (1993) demonstrated using simple coupled models that the delayed oscillator is a mixture of SST and ocean dynamics modes; in that regard, the point we wish to suggest is that the R15 coupled model is in Jin and Neelin's ''mixed SST/ocean dynamics mode'' regime, rather than the pure SST mode limit.] In the earlier assessments, westward propagation of SST anomalies on the 2–4-yr timescale, as noted by Lau et al. (1992) for a similarly constructed R15 coupled model, was cited as evidence for the SST mode interpretation. We have also found, based on time-longitude diagrams of bandpass-filtered SST (not shown), that westward phase propagation occurs frequently in our model on the 2–4-yr timescale, although events with eastward propagating or stationary anomalies also occur. However, for the 4–7-yr band and at longer periods, the westward SST phase propagation is less pronounced and occurs much less frequently. Hence in the SST life cycle for the 2–7-yr band as a whole (Figs. 3, 4) the westward phase propagation appears quite limited, with the composite evolution pattern being quasi-stationary. Furthermore, the results in Fig. 5 indicate that the coherence between central Pacific

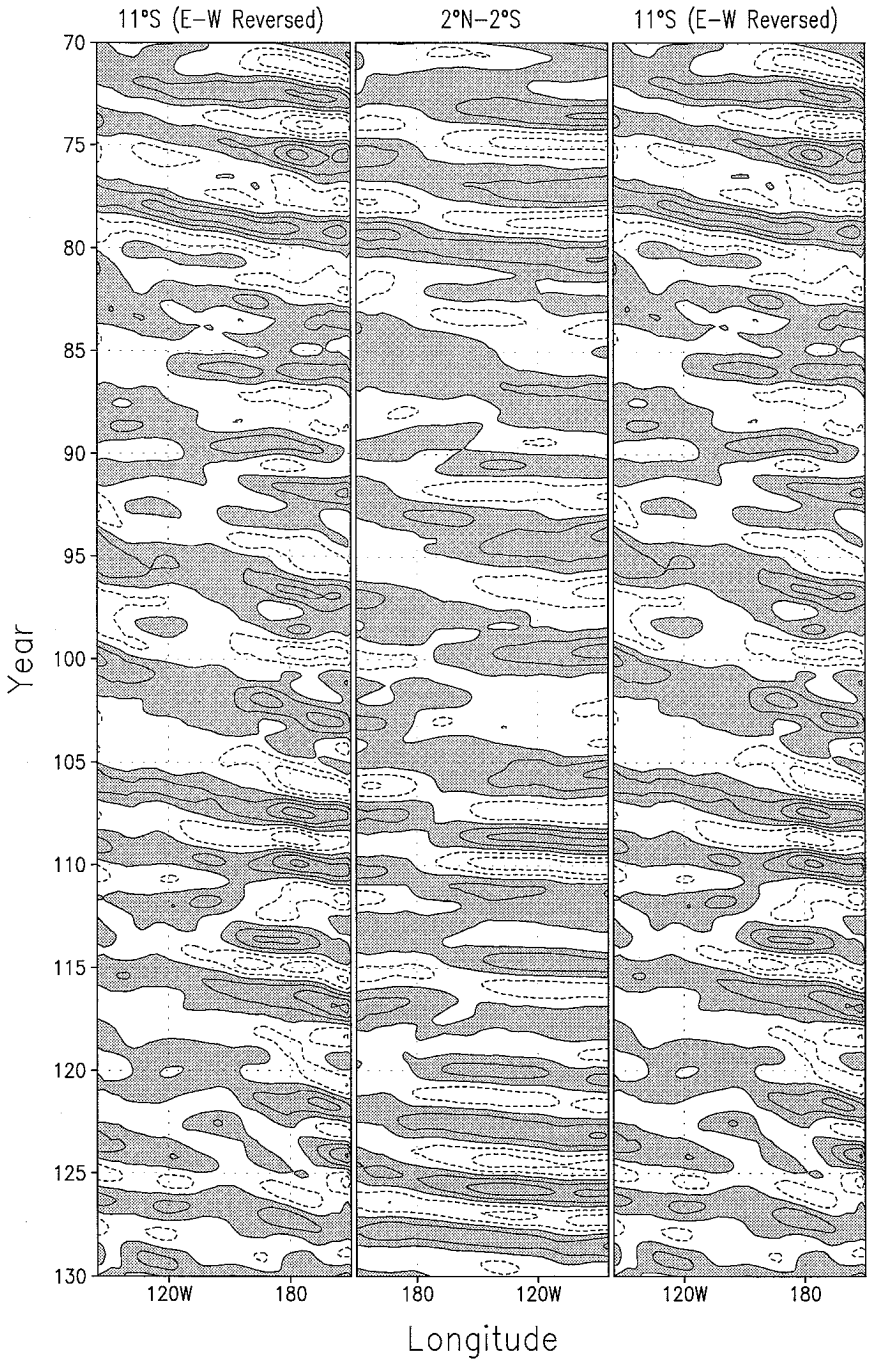

FIG. 6. Time–longitude diagrams of ocean heat content anomalies (51–595 m vertically integrated; 2–7 yr bandpass filtered) over the tropical Pacific for years 70–130 of the control experiment. The middle panel shows anomalies averaged 2°N–2°S, whereas the left and right panels show anomalies at 11°S. Note that the longitudes have been reversed on the (identical) left and right panel so that shading progressing from upper left to lower right indicates a westward propagating signal at 11°S, whereas on the middle panel it indicates an eastward propagating signal along the equator. The contour interval is 50 K m, with positive anomalies shaded.

SST and western Pacific subsurface heat content is a maximum at about 5–6 yr, and becomes much less significant at periods less than 3 yr. These results suggest that the interpretation of the model's phenomenon as an SST mode in earlier assessments resulted in part because the assessments were based on a limited period range (2–4 yr) for which westward SST propagation is more pronounced in the model. On the other hand, analysis of the 2–7 yr band—which includes the periods (5–6 yr) for which the surface–subsurface coherence is most pronounced—clearly indicates that the subsurface ocean evolution plays an important role in the R15 model ENSO, from which we conclude that the model is probably in the mixed SST–ocean dynamics mode regime.

e. Higher frequency (<18 month) model fluctuations

Whereas the heat content anomalies described above propagate much more slowly than free (uncoupled) Kelvin and Rossby waves (Philander et al. 1992), it is of interest to briefly discuss the model's behavior on the much shorter timescales (<18 months) characteristic of uncoupled equatorial Kelvin and Rossby modes. As noted previously in the coherence spectrum results (Fig. 5), SST in the central equatorial Pacific and subsurface heat content in the western tropical Pacific are less correlated on timescales less than 18 months than on longer (>2 yr) timescales. Time–longitude diagrams of subsurface heat content for the <18 month band (not shown) indicate the occurrence of crudely resolved versions of the uncoupled eastward propagating Kelvin and westward propagating Rossby modes identified in the much higher resolution GCM simulation of Philander et al. (1992). These features have similar phase speeds but roughly one-half the amplitude of the uncoupled modes discussed in the Philander et al. study. Thus, despite its very coarse resolution, our ocean model, which has zonal and meridional velocity grid points located on the equator, appears to at least crudely resolve the uncoupled, higher frequency Kelvin and Rossby modes.

4. Wavelet analysis of amplitude modulation

An understanding of how ENSO has varied in the past provides an important context for an examination of the possible impact of increased CO_2 on the amplitude of ENSO. It is now well established that the amplitude of ENSO has varied substantially during the past century (e.g., Fig. 1b; Gu and Philander 1995 and references therein). However, the multicentury $\delta^{18}O$ record of Dunbar et al. (1994) presents an opportunity to examine the amplitude of ENSO over the past three and a half centuries and to compare its variation to that in our 1000-yr coupled model integrations.

In this section, the wavelet analysis technique of Gu and Philander (1995) is used to analyze both the $\delta^{18}O$ record and model time series of SST. The reader is referred to the Gu and Philander study for a mathematical description of the wavelet formulation used in the analysis. Details of the wavelet analysis method can be found in the book by Combes et al. (1989) and in the review by Farge (1992). In brief, the wavelet technique can be used to obtain information on the *temporal evolution* of the amplitude of fluctuations for a given frequency or frequency range. The method involves projecting the time series onto wavelets, consisting of the stretched or compressed form of a ''mother wavelet.'' For this analysis the mother wavelet used is the Morlet wavelet, consisting of sinusoidal functions modulated by a Gaussian envelope with large amplitude near the center of the wavelet and negligible amplitude far away from the center. The wavelets are passed through the data to obtain the temporal evolution of the amplitudes for given periods. The width of the mother wavelet is specified by the investigator according to the time resolution desired, amount of data available, purpose of the analysis, etc.

Wavelet amplitudes or variance can be displayed in two-dimensional form (as a function of both time and frequency) or in one-dimensional form (as a function of time and aggregated across a range of frequencies). The two-dimensional form allows one to examine the time evolution of the variance spectrum. This technique is similar in some respects to evolutionary or ''moving-window'' spectral analysis (used, e.g., by Dunbar et al. 1994), although with some important differences. In evolutionary spectral analysis, spectra are computed for different overlapped subsegments of the full time series, with the subsegments determined using a moving fixed-width window through the time series. This results, for each subsegment, in a relatively small sample of events within the window at lower frequencies and a larger sample of events at higher frequencies. In contrast, with wavelet analysis the effective width of the ''moving window'' varies with frequency, being wider for lower frequencies and narrower for higher frequencies (essentially sampling the same number of oscillations for each frequency considered). By use of this frequency-dependent window width, the wavelet method can provide relatively high time resolution at higher frequencies, while at the same time avoiding giving less reliable results based on relatively few events at lower frequencies. In addition, wavelet transforms conserve information from the original series, both locally and globally (Gu and Philander 1995), while the moving-window Fourier transforms do not. Owing to these advantages of the wavelet technique, we have chosen to use it to explore the multidecadal fluctuations of ENSO amplitude and frequency in this study.

a. Results: Two-dimensional wavelet analysis

Figure 7 shows a two-dimensional plot of wavelet variance as a function of frequency and time for the

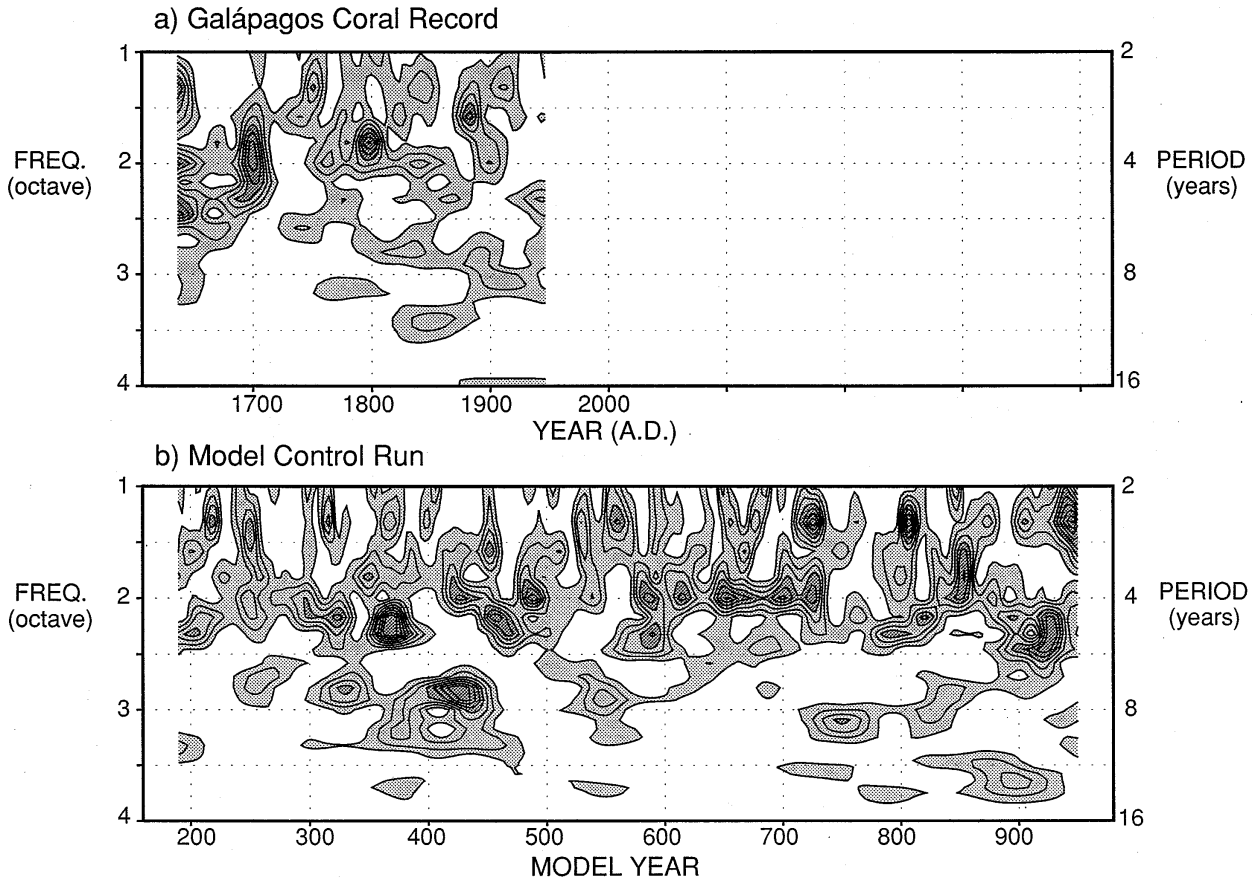

FIG. 7. Two-dimensional representation of wavelet variance as a function of period (i.e., frequency^{-1}) and time (see text) for (a) the δ^{18}O coral record of Dunbar et al. (1994) and (b) model control run SST (7°N–7°S, 173°E–120°W). For the coral data (a) the contour interval is 0.05 K^2 yr^{-1} with values greater than 0.05 (0.2) indicated by light (dark) shading; for the model, the contour interval is 0.005 K^2 yr^{-1} with values greater than 0.005 (0.02) indicated by light (dark) shading.

δ^{18}O record and R15 model control run. In the notation of Gu and Philander, the quantity plotted is

$$\frac{|\tilde{f}(t', a)|^2}{a^2}, \qquad (1)$$

where $\tilde{f}(t', a)$ is the wavelet coefficient; t' is the translation parameter corresponding to the position of the (moving) wavelet in the time series; and a is the scale dilation parameter that represents the period (or frequency). In this form, the integral of (1) over all values of a gives the total variance at time t'. In the present study, a larger Gaussian envelope width parameter (by a factor of 2.5) is used than in Gu and Philander (1995), which results in a smoother evolution curve for the wavelet amplitudes. (Note in Fig. 7 that the contour interval for Fig. 7a is 10 times that for Fig. 7b, reflecting the much lower interannual SST variance in the model compared to that inferred for the real-world eastern equatorial Pacific.)

In the δ^{18}O record, (Fig. 7a) pronounced episodes of high variance and strong amplitude modulation are evident in the period range of about 3–6 yr. For the control simulation (Fig. 7b) episodes of high variance and strong amplitude modulation tend to be clustered in roughly the 2–6-yr period range. The 2–6-yr range is broadly consistent with estimates of the predominant timescale of ENSO by a number of investigators (e.g., Trenberth 1976; Diaz and Pulwarty 1994; Dunbar et al. 1994). The results in Fig. 7a also indicate that within the 2–6 yr band the spectral peaks associated with ENSO have shifted toward slightly higher frequencies over the past few centuries, a feature also noted by Dunbar et al. (1994) for the Galápagos δ^{18}O data. [See also Michaelsen (1989), Enfield and Cid S. (1991), and Diaz and Pulwarty (1994) for analyses of the temporal evolution of spectral peaks in several other long-term ENSO-sensitive indices].

One feature of the model results (Fig. 7b) that is not also evident in the δ^{18}O results is the occasional sporadic concentration of variance in the decadal range (~7–15 yr periods). This feature is quite variable from century to century in the model, which suggests that the δ^{18}O record may be too short to adequately sample the 7–15-yr variability. Diaz and Pulwarty (1994) found ev-

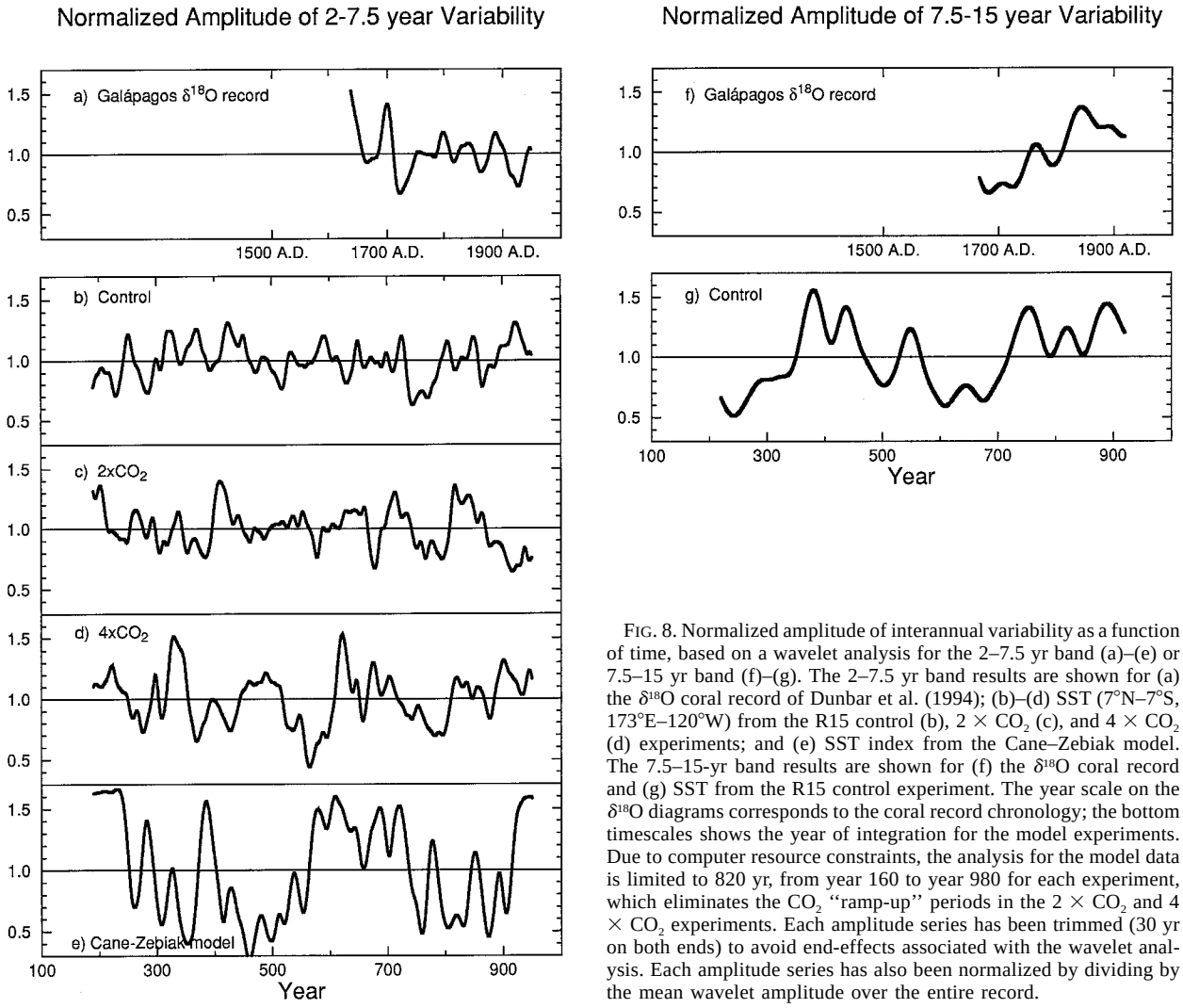

FIG. 8. Normalized amplitude of interannual variability as a function of time, based on a wavelet analysis for the 2–7.5 yr band (a)–(e) or 7.5–15 yr band (f)–(g). The 2–7.5 yr band results are shown for (a) the δ^{18}O coral record of Dunbar et al. (1994); (b)–(d) SST (7°N–7°S, 173°E–120°W) from the R15 control (b), 2 × CO_2 (c), and 4 × CO_2 (d) experiments; and (e) SST index from the Cane–Zebiak model. The 7.5–15-yr band results are shown for (f) the δ^{18}O coral record and (g) SST from the R15 control experiment. The year scale on the δ^{18}O diagrams corresponds to the coral record chronology; the bottom timescales shows the year of integration for the model experiments. Due to computer resource constraints, the analysis for the model data is limited to 820 yr, from year 160 to year 980 for each experiment, which eliminates the CO_2 "ramp-up" periods in the 2 × CO_2 and 4 × CO_2 experiments. Each amplitude series has been trimmed (30 yr on both ends) to avoid end-effects associated with the wavelet analysis. Each amplitude series has also been normalized by dividing by the mean wavelet amplitude over the entire record.

idence for substantial variability in ENSO-sensitive indices on decadal and longer scales during the past 1000 yr, although they noted that these features were not present throughout the records nor present consistently among different indices.

The results in Fig. 7 suggest that the amplitude modulation characteristics of the interannual (~2–6 yr) timescale are quite different from those on the decadal timescale (>7 yr) for both the model and the δ^{18}O data. Based on this result—as well as other cross spectral and spectral analysis results (e.g., Fig. 5 and results to be presented later in section 5) suggesting the possible existence of a coherence minimum or a "spectral gap" at about 7-yr period for the model—the interannual (~2–7 yr) and decadal (~7–15 yr) bands are analyzed separately in this report. For example, CO_2 sensitivity results for SST variability in each band are presented separately in order to demonstrate that our general conclusions (except as noted) are not strongly sensitive to the particular timescale range selected. Improved understanding of the relationship between the interannual (2–7 yr) and decadal (7–15 yr) scale fluctuations remains as a topic for future study for both the model and the real world.

b. Results: One-dimensional wavelet analysis

Normalized wavelet coefficients, integrated over the 2–7.5 yr and 7.5–15 yr bands, respectively, were computed to compare the relative amplitude modulation in various models and the δ^{18}O record more clearly. Amplitude time series for the 2–7.5-yr band are shown in Figs. 8a–d for the δ^{18}O record and the R15 experiments (control, 2 × CO_2, and 4 × CO_2). Although most of our ENSO–CO_2 sensitivity results are presented in the next section, we briefly examine the impact of increased CO_2 on the amplitude modulation behavior in this section. As an additional comparison, the 2–7.5 yr amplitude series is shown (Fig. 8e) for an 820-yr SST record from the Cane–Zebiak coupled model (data kindly pro-

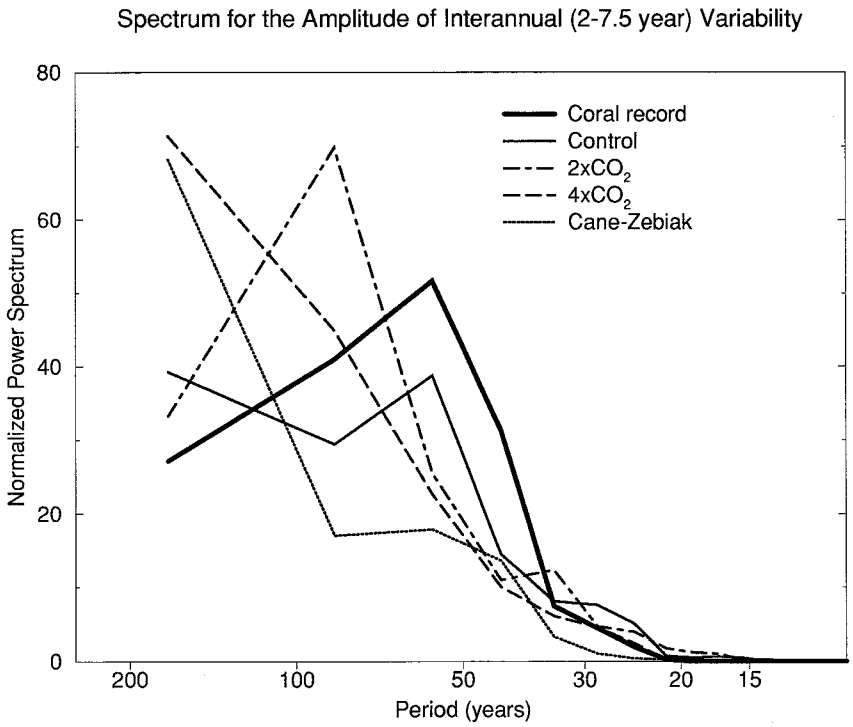

FIG. 9. Normalized power spectra of the wavelet amplitude time series (2–7.5-yr band) in Figs. 8a–e. See legend to identify individual models or datasets. The spectra were computed by averaging spectra from a series of partially (50%) overlapped subsegments of the full amplitude time series. For the 820-yr model time series, a series of seven overlapped subsegments of length 2048 months were used; for the $\delta^{18}O$ record a series of three overlapped subsegments of length 2048 months were used. The input time series were the mean-normalized series shown in Figs. 8a–e, which were subsequently divided by their respective standard deviations before computing the spectra.

vided by S. Zebiak). The Cane–Zebiak model's ENSO is known to exhibit marked temporal variations in amplitude (Zebiak and Cane 1991).

As an alternative form of presenting the results (i.e., in the frequency domain rather than the time domain), in Fig. 9 are shown the normalized power spectra for each of the mean-normalized 2–7.5-yr wavelet amplitude series from Figs. 8a–e. Although the bandwidth and confidence limits of these spectra are large (not shown), the results give a general indication of the preferred timescale for the amplitude modulation behavior, at least for the available data records.

The amplitude results for the $\delta^{18}O$ record (Fig. 8a) show a fairly regular fluctuation of amplitude and suggest a preferred timescale of about 60 yr (Fig. 9). These features were also apparent in the two-dimensional wavelet results (Fig. 7a). Of particular note in Fig. 8a is the period of relatively large SST variability (high amplitude) around 1880–1910 followed by lower amplitudes in the 1920s and 1930s and by a return toward higher values for the final decades shown (around 1950). This behavior is broadly consistent with the wavelet analysis of instrumental data for the last century (Gu and Philander 1995; see also Fig. 1 of the present study). Another intriguing feature of the $\delta^{18}O$ record is the pronounced fluctuation in ENSO amplitude occurring from the beginning of the record to around 1750. The large magnitude of these amplitude changes suggests that despite the substantial variation in ENSO's amplitude observed during the past century, even *larger* multidecadal-scale variations in ENSO amplitude may have occurred in the 1600s and 1700s.

For the R15 control run (2–7.5 yr band), the normalized amplitude series (Fig. 8b) also shows substantial amplitude modulations. However, while a small peak appears in the spectrum of the time series at about 60-yr period (Fig. 9), this peak is much less pronounced than that in the $\delta^{18}O$ spectrum. The substantial multidecadal amplitude fluctuations in the control run are entirely internally generated in the model, which suggests that much of the amplitude modulation for the observed ENSO (as inferred from the coral data) may be attributable to internally generated variability, as opposed to being externally forced (e.g., by solar variations, volcanos, etc.).

In terms of the typical relative size of the amplitude modulation, the standard deviation of the mean-normalized $\delta^{18}O$ amplitude series (σ_n) in Fig. 8a is 0.16. In comparison, σ_n for the R15 model amplitude series in Fig. 8 are 0.15 (control experiment), 0.16 ($2 \times CO_2$),

and 0.21 ($4 \times CO_2$). The relative amplitude changes in the Cane–Zebiak series (Fig. 8e) are the largest of any of the series shown ($\sigma_n = 0.40$). The increase in relative size of the amplitude modulation between the control and $4 \times CO_2$ experiments is statistically significant, according to a comparison of (unnormalized) spectra for the mean-normalized amplitude series (not shown). Specifically, we removed linear trends from the mean-normalized wavelet amplitude series for the control and $4 \times CO_2$ experiments (shown in Fig. 8b,d) and accumulated the variance in each detrended series over the first 15 calculable Fourier frequencies, encompassing periods of 50 yr and greater. The accumulated variance estimate for the $4 \times CO_2$ series lies above the 95% confidence limits for that of the control run.

The (normalized) spectra results in Fig. 9 for the R15 coupled model also suggest that as the CO_2 content increases (e.g., from control to $2 \times CO_2$ to $4 \times CO_2$), the dominant *timescale* of the amplitude modulation becomes progressively longer, and the spectra become redder. The longest modulation timescale and reddest spectrum in the available samples occurs for the Cane–Zebiak model. The $\delta^{18}O$ record appears to be too short to determine which type of modulation behavior (R15 control run or Cane–Zebiak) is more ''realistic'' (assuming the modulation in the $\delta^{18}O$ record accurately captures the modulation of the real ENSO). However, on the basis of the record available thus far the amplitude modulation in the Cane–Zebiak model (2–7.5-yr band) appears to occur on a substantially longer timescale than that in the $\delta^{18}O$ data.

In the second part of Fig. 8 (panels f, g), the one-dimensional wavelet amplitude results for the *7.5–15 yr* variability are shown. Results are shown only for the $\delta^{18}O$ and R15 control run data. For both these time series, the amplitude modulation occurs on a substantially longer timescale (>100 yr) for the 7.5–15 yr variability than for the 2–7.5 yr variability (Figs. 8a,b). This feature is also evident in the two-dimensional wavelet results (Fig. 7).

Overall, the one-dimensional wavelet results in Figs. 8 and 9 indicate that the amplitude of ENSO varies substantially on multidecadal timescales in both models and the real world. The results suggest that even a fairly substantial CO_2-induced change in ENSO amplitude (say 30%) may be difficult to distinguish from this modulation ''noise'' unless either the data record is quite long (perhaps several centuries) or one is somehow able to mechanistically separate the natural and anthropogenic influences on ENSO variability.

5. Impact of increased CO_2 on ENSO-like fluctuations

In this section the impact of increased CO_2 on various aspects of the coupled model's ENSO is examined. In both the real world and in models, ENSO appears to exhibit substantial multidecadal to multicentury amplitude modulation (which itself appears to be sensitive to increased CO_2, as noted in the previous section). Therefore, climate change sensitivity experiments may require integrations on the order of several hundred years to separate a CO_2-induced impact on ENSO variability from internal noise. Our coupled model, despite its weak interannual variability, nevertheless appears to capture the essential physical mechanism of ENSO. The amplitude of ENSO increases to more realistic values in higher resolution versions of this model (e.g., Philander et al. 1992), but at the expense of much higher computational requirements. It has not been feasible thus far to carry out multicentury climate integrations using such a high resolution model. It is therefore apparent that our low resolution model is a better choice for carrying out such CO_2–ENSO sensitivity experiments at this time.

a. CO_2 sensitivity of model SST variability

The experimental design for the CO_2 sensitivity runs with the coupled model is depicted in Fig. 10a, which shows the log of CO_2 concentration in the model, relative to present-day levels, for each experiment. The control experiment has constant CO_2 at present levels for 1000 yr, while in the $2 \times CO_2$ ($4 \times CO_2$) experiment, CO_2 gradually increases to twice (four times) the present level over a period of 70 (140) years, then remains at that elevated level for the remainder of the 1000-yr integration. The global surface air temperature response to the increased CO_2 is shown in Fig. 10b. Most of the global warming occurs during the CO_2 buildup period, although global temperature continues to increase slowly even after 1000 yr, owing to the very long timescales in the model's coupled ocean–atmosphere ice system (Manabe and Stouffer 1994). Although not shown here, the tropical Pacific warms by about 4°C during the first 150 yr of the $4 \times CO_2$ experiment (Knutson and Manabe 1994), and the time-mean zonal contrast in SST along the equator decreases by about 20% after roughly 300 yr in the $4 \times CO_2$ experiment (Knutson and Manabe 1995).

Figures 10c–e shows the temporal evolution of the standard deviation of bandpass-filtered SST, obtained by computing the standard deviation for overlapped multiyear segments running through the data. Results are shown for SST averaged over the SST reference region (7°N–7°S, 173°E–120°W), although similar results are obtained using the first principal component of Pacific SST over the domain 40°N–40°S (not shown). The ''moving window'' standard deviation technique is used here, rather than wavelet analysis (section 4) because the focus is on CO_2-induced changes in amplitude, rather than the internal multidecadal amplitude modulation. For example, using a wide (100-yr) moving window, as in Fig. 10c, smooths out most of the multidecadal amplitude modulations, whereas attempts to obtain similarly smooth curves using the wavelet technique would

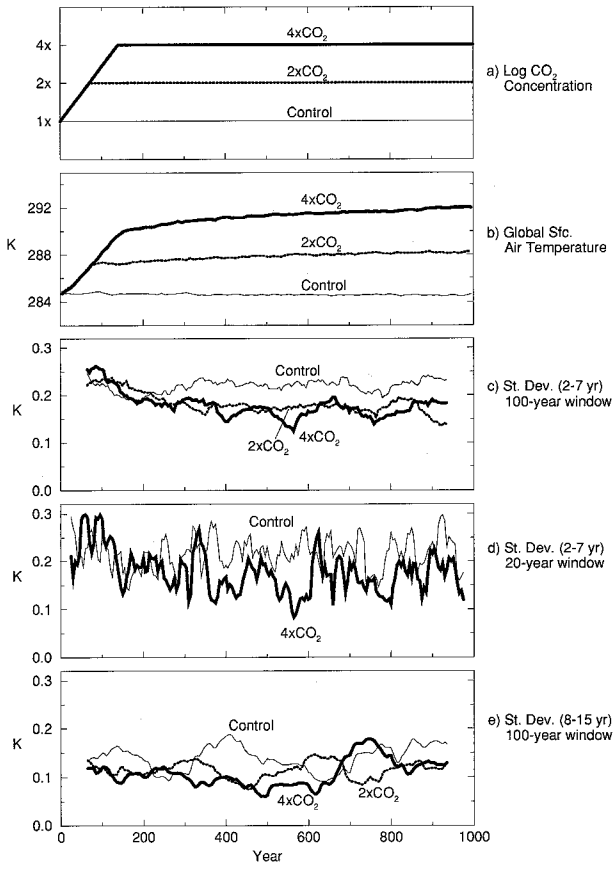

FIG. 10. Time series of (a) log of CO_2 concentration relative to present day values; (b) global surface air temperature decadal means; (c), (d) running standard deviation of 2–7-yr filtered SST (7°N–7°S, 173°E–120°W) obtained using a moving window of width 100 yr (c) or 20 yr (d); and (e) as in (c) but for 8–15-yr filtered data. Values are plotted at the centerpoint of the window. The light lines in each diagram correspond to the control experiment, the dotted lines to the $2 \times CO_2$ experiment [not plotted in (d)], and the dark lines to the $4 \times CO_2$ experiment. Units are K for (b)–(e).

require much larger truncation of the output series (several centuries) due to end effects.

The results in Fig. 10c show that after an initial adjustment period lasting roughly 250 yr, the $4 \times CO_2$ and $2 \times CO_2$ standard deviation curves remain below the control experiment curve for the remainder of the 1000-yr integrations. Comparing years 16–985 for the control with years 201–985 for the $2 \times CO_2$ and $4 \times CO_2$ experiments, the 2–7 yr SST standard deviation for the region decreases by 22.7% for $4 \times CO_2$ and by 21.5% for $2 \times CO_2$. It is not clear why the $2 \times CO_2$ and $4 \times CO_2$ results are not more different from each other; we suspect that sampling variability remains a problem even with 1000-yr simulations.

The running standard deviation obtained using a narrower (20-yr) window (Fig. 10d) retains much of the multidecadal amplitude modulation and thus the curves are similar to those of the 1D wavelet analysis in Fig. 8 (apart from the normalization applied in Fig. 8). Figure 10d clearly shows the larger magnitude of the multidecadal amplitude modulations in the $4 \times CO_2$ versus control experiment, as well as the reduction in the ''average'' standard deviation level in the $4 \times CO_2$ case. Note that the ~20% reduction in the standard deviation due to a quadrupling of CO_2 is similar in magnitude to the multidecadal amplitude modulations in Fig. 10d (see also section 4b). This suggests that the detection of a CO_2-induced change in ENSO amplitude in the real world could be complicated considerably by the presence of substantial internally generated amplitude modulations.

The results in Figs. 10c and 10d also illustrate some potential problems with relying on relatively short records (of either modeled or observed data) for assessing CO_2 impacts on ENSO. For example, Tett's (1995) modeling results (see his Fig. 21b) for a pair of 75-yr transient experiments would correspond roughly to the results shown for the first century alone in Fig. 10d. The results for the first century in our Fig. 10d show no clear CO_2 signal (similar to Tett's conclusion) yet using a longer (1000-yr) integration and wider (100-yr) window (e.g., Fig. 10c) reveals that in our model a 20% decrease in standard deviation (and roughly a 40% decrease in variance) occurs with $4 \times CO_2$. Thus, it seems possible that a CO_2–ENSO sensitivity of *at least* that magnitude (and of *either sign*) could still be revealed in a longer integration of the Hadley Centre coupled model. Similarly, Meehl et al. (1993) analyzed an even shorter sample of model output (15 yr of data from both a control and $2 \times CO_2$ experiment with an NCAR coupled model), and thus their study could say nothing definitive about ENSO amplitude, other than that the amplitude did not appear to change appreciably over the very short period analyzed. Meehl et al.'s study was focused mainly on possible changes in ENSO related effects, such as precipitation anomalies, assuming SST anomalies of a similar size in the control and CO_2-warmed climates.

In Fig. 10e are the running mean standard deviations for the *8–15-yr* band of the spectrum. As noted in section 4, pronounced fluctuations in the amplitude of 8–15 yr fluctuations occur on a multicentury timescale in the model. This very long timescale modulation obscures the CO_2-induced signal, despite the use of a wide (100-yr) window. However, using the full data records (years 16–985 from the control run versus years 201–985 from the $2 \times CO_2$ and $4 \times CO_2$ experiments) the percentage changes in the standard deviation are −19.8% ($4 \times CO_2$) and −18.0% ($2 \times CO_2$), which are similar to the percentage changes estimated for the 2–7-yr band.

To assess the statistical significance of the CO_2-induced decreases in SST variability in the model, variance spectra were computed for the SST reference time series using the last 840 yr of both the control and $4 \times CO_2$ experiments (Fig. 11). Prior to computing the spectra, a cubic polynomial trend was removed from

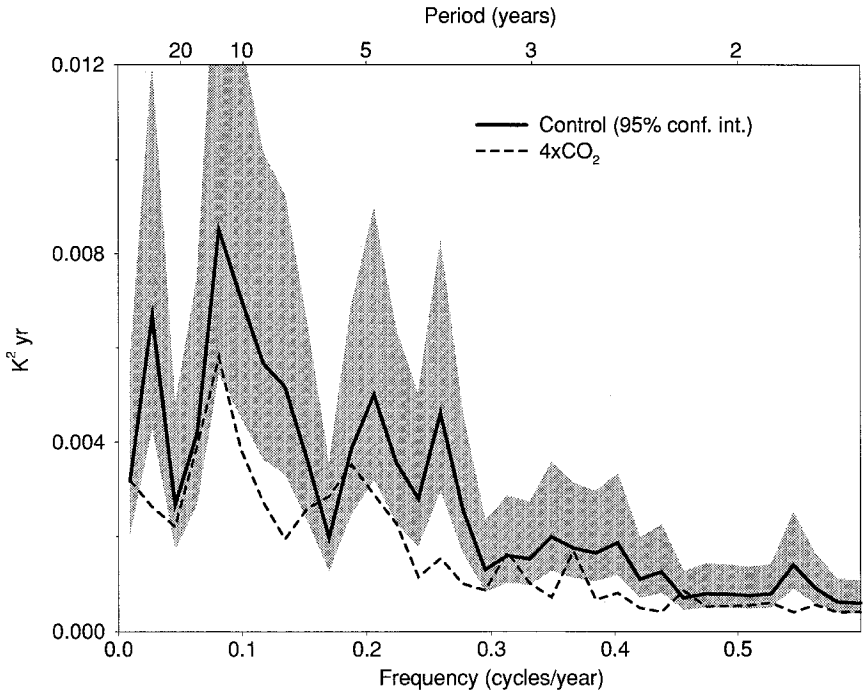

FIG. 11. Variance spectra of SST (7°N–7°S, 173°E–120°W) from the control and 4 × CO_2 experiments (years 161–1000). A least-square cubic polynomial curve was subtracted from each series prior to computing the spectra. The raw spectra were smoothed using a nonoverlapping rectangular window of width 15 calculable frequencies. The shaded region indicates the 95% confidence bounds (Chatfield 1975) for the control run spectrum.

both time series, a step that was necessary in the 4 × CO_2 case due to the continued gradual (nonlinear) warming trend in the model, which follows the rapid warming of the first 160 yr. The shading in Fig. 11 depicts the 95% confidence intervals for the control run spectra as obtained using a nonoverlapping rectangular window of width 15 calculable frequencies (e.g., Chatfield 1975). Note that most of the 4 × CO_2 spectrum lies below the control run spectrum, and that a substantial fraction of the 4 × CO_2 estimates fall beneath the 95% confidence limits for the control run spectrum. These results indicate that the CO_2-induced decrease in the model ENSO's SST variability is statistically significant.

A preliminary assessment of the impact of increased CO_2 on the *frequency* of the model's ENSO events can also be obtained from Fig. 11. The variance spectra for both the control and 4 × CO_2 cases have peaks at periods of about 5 and 12 yr. A third peak near a 4-yr period in the control run is not present in the 4 × CO_2 case. However, most of the main features in the spectra appear similar for the two cases (over the 2–15 yr band).

An alternative way of describing the model ENSO and its CO_2-induced changes is by fitting the model SST time series used for Fig. 11 with an autoregressive model of order (n) [i.e., an AR(n) model]. The AR(n) model is of the form

$$y(t) = \sum_{\nu=1}^{n} \alpha_\nu y(t - \nu\,\delta t) + \xi(t), \qquad (2)$$

where $\xi(t)$ is a Gaussian white noise process and δt is a time increment (e.g., see Wilks 1995). For two-month averaged anomaly series from the R15 control run, an AR(2) model describes the time series sufficiently well to pass a Portmanteau test (e.g., Honerkamp 1994) at the 0.05 significance level. For the control run series, the maximum likelihood estimates for the AR(2) parameters (α_1, α_2) are (1.047 ± 0.027, −0.210 ± 0.027), where the ± ranges denote 95% confidence limits. For the 4 × CO_2 run, the corresponding AR(2) parameters are (1.116 ± 0.027, −0.260 ± 0.027). The differences between the estimated parameters for the control and 4 × CO_2 experiments are small but statistically significant. For both the control and 4 × CO_2 time series, the AR(2) parameters indicate the presence of decaying modes in the model, rather than oscillatory modes (Honerkamp 1994, 426–430). A possible physical interpretation of this result, based on the analysis of Chang et al. (1996), is that the GFDL R15 model ENSO may result from stable dynamics driven by stochastic processes.

In Fig. 12 are maps of the standard deviation of 2–7-yr filtered SST from the control run (years 16–985), 4 × CO_2 run (years 201–985), and the difference between the two maps. Fifteen years of data have been

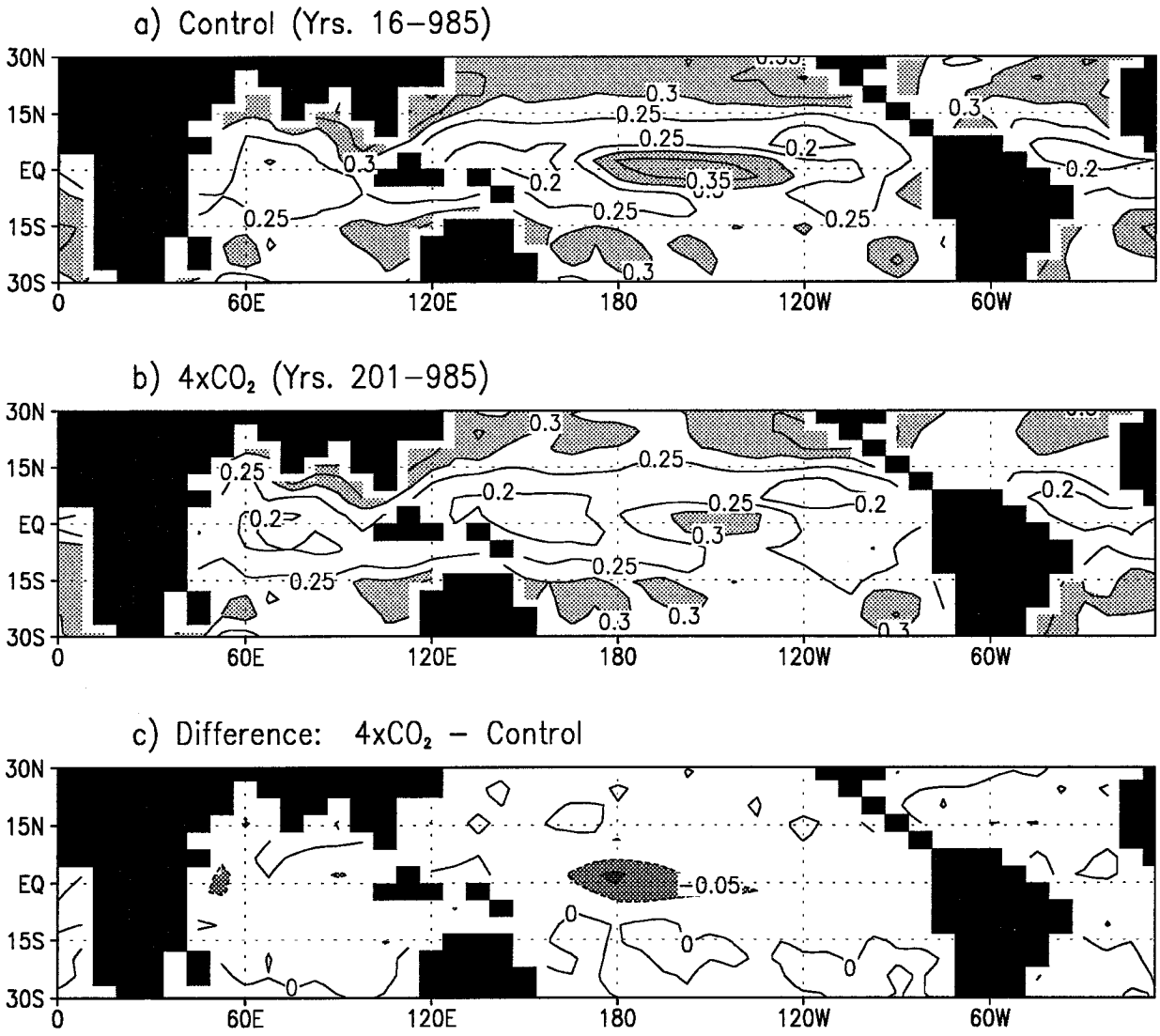

FIG. 12. Maps of the standard deviation of SST (2–7-yr filtered data) from (a) the control experiment, years 16–985; (b) the 4 × CO_2 experiment, years 201–985; and (c) the difference (b − a). Contour interval is 0.05°C, with values greater than 0.3°C shaded.

lost from the beginning and end of the data records due to end effects of the bandpass filter. In addition, the first 200 yr of the 4 × CO_2 experiment have been excluded to reduce the effects of the transient adjustment to the 4 × CO_2 forcing (Fig. 10). The control run map (Fig. 12a) shows a local maximum in SST variability in the central equatorial Pacific corresponding approximately to the region used to obtain the SST reference series in this study. This feature is also present in a similar map for the 8–15-yr band (not shown). The magnitude of this equatorial maximum in 2–7-yr variability is clearly reduced in the 4 × CO_2 experiment (Fig. 12b vs 12a). The region of maximum variability also shifts eastward slightly, with the largest change occurring near the date line (Fig. 12c), at the western edge of the region of enhanced variability in the control run. A similar decrease in variability occurs in this region for the 8–15 yr band (not shown). Thus, apart from the pronounced multicentury amplitude modulation for the 8–15 yr band (Fig. 10e), the CO_2 responses appear to be similar in the 2–7 and 8–15 yr bands.

b. CO_2 sensitivity of simulated ENSO precipitation and surface wind anomalies

In this section, the precipitation and surface wind anomalies associated with the model ENSO's SST anomalies are compared for the control and 4 × CO_2 experiments. Figure 13 shows the precipitation and surface wind linear regression anomalies for a 1°C SST anomaly over the region 7°N–7°S, 173°E–120°W in each experiment. Results shown are for the 2–7 yr band and zero lag.

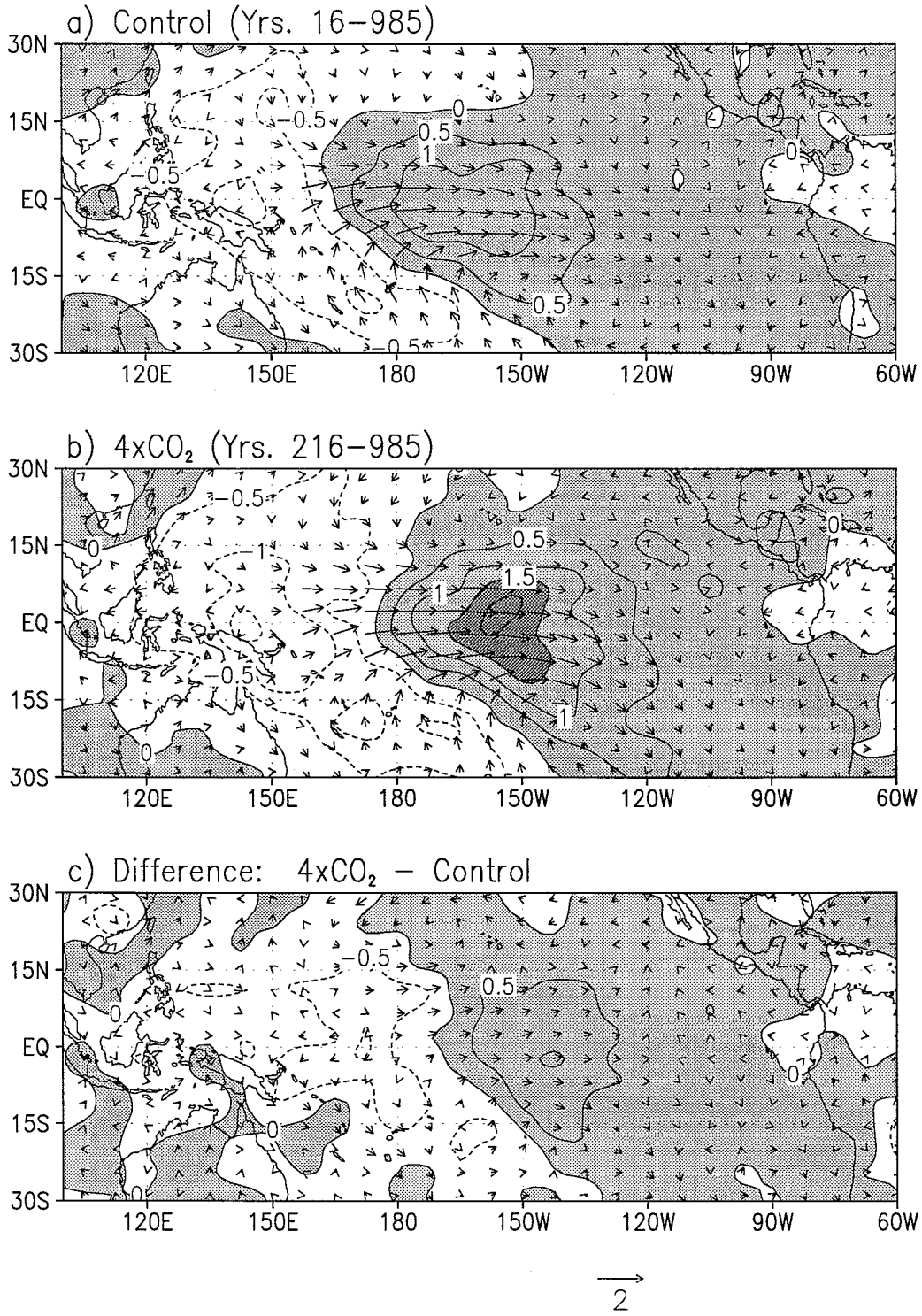

FIG. 13. Linear regression of precipitation (contours, shading) and surface wind (vectors) anomalies vs SST (7°N–7°S, 173°E–120°W) for (a) the control experiment, years 16–985; (b) the 4 × CO_2 experiment, years 201–985; and the difference (b − a). The data used are 2–7-yr band-pass filtered. Contours are 0.5 mm day^{-1} $°C^{-1}$, with positive values shaded. The vector scale (in m sec^{-1} $°C^{-1}$) is shown beneath the diagram.

In the control experiment (Fig. 13a) a large region of positive precipitation anomalies occurs in the central equatorial Pacific at the time of maximum SST, accompanied by negative precipitation anomalies over much of the western Pacific warm pool region and Indonesia. This pattern resembles the observed ENSO-related precipitation anomaly pattern for the tropical Pacific obtained by Ropelewski and Halpert (1987).

In the 4 × CO_2 experiment, the peak positive precipitation anomalies (per °C) are about 50% stronger than in the control experiment (Figs. 13b,c). Averaged over a large region of the central equatorial Pacific (11°N–11°S, 173°E–113°W), the precipitation anomaly (per °C) is about 24% larger in the 4 × CO_2 experiment than in the control. This pronounced intensification of the positive precipitation anomalies (per °C) is associated with the very large (i.e., 45%) increase in the time-mean vertically integrated water vapor content of air and increased evaporation rates in the 4 × CO_2 experiment. The increased moisture allows for a greater increase in moisture convergence (for a given circulation anomaly) over the central equatorial Pacific during ENSO warm episodes and thus enhances the precipitation anomaly (per °C) in that region. Meehl et al. (1993) also found, using an NCAR GCM, that central equatorial Pacific precipitation anomalies (for a given SST anomaly) were enhanced in a CO_2-warmed climate, suggesting that a similar mechanism operates in their model. The regression difference field (Fig. 13c) shows areas of both increase and decrease, indicating a tendency for the precipitation anomalies in the 4 × CO_2 experiment to be shifted eastward (by about one grid point, or 7.5° longitude) relative to those in the control run.

The wind anomalies at the time of peak ENSO warming in both experiments (Figs. 13a,b) indicate a net weakening of the trade winds and equatorial easterlies, as occurs with the observed ENSO (e.g., Rasmusson and Carpenter 1982). However, the wind regression anomalies (per °C) are only slightly stronger in the 4 × CO_2 experiment (Fig. 13c), despite the much stronger intensification of the peak precipitation anomalies noted above. Thus, the much stronger peak convective heating anomalies (per °C) implied by the more intense precipitation anomalies (per °C) do not lead to similar increases in the surface wind anomalies (per °C).

Note that although the precipitation *regression* anomalies for a central equatorial Pacific rainfall index (11°N–11°S, 173°E–113°W) increase by 24% in the 4 × CO_2 experiment for a given SST anomaly, the *net* interannual variability of precipitation in the region increases only slightly (Knutson and Manabe 1994). This is because the increase in precipitation regression anomalies (per °C) is mostly offset by the decrease in SST variability.

c. Heat balance perspective on the CO_2 response

An interesting question concerning the simulated CO_2 response of ENSO is why the surface wind anomalies (per °C) are only slightly stronger in the 4 × CO_2 case, despite the much more enhanced precipitation anomalies (per °C) in the warmer climate. To examine this question from a heat balance perspective, in Fig. 14 is the regression of various tropospheric heat balance components versus the SST reference series. The heat balance terms shown are area averages for the region 11°S–11°N, 173°E–113°W and are shown for tropospheric levels from 940 to 205 mb; at higher levels (e.g., 95 mb) the condensation heating anomalies are negligible.

The tropospheric heating anomaly due to moist con-

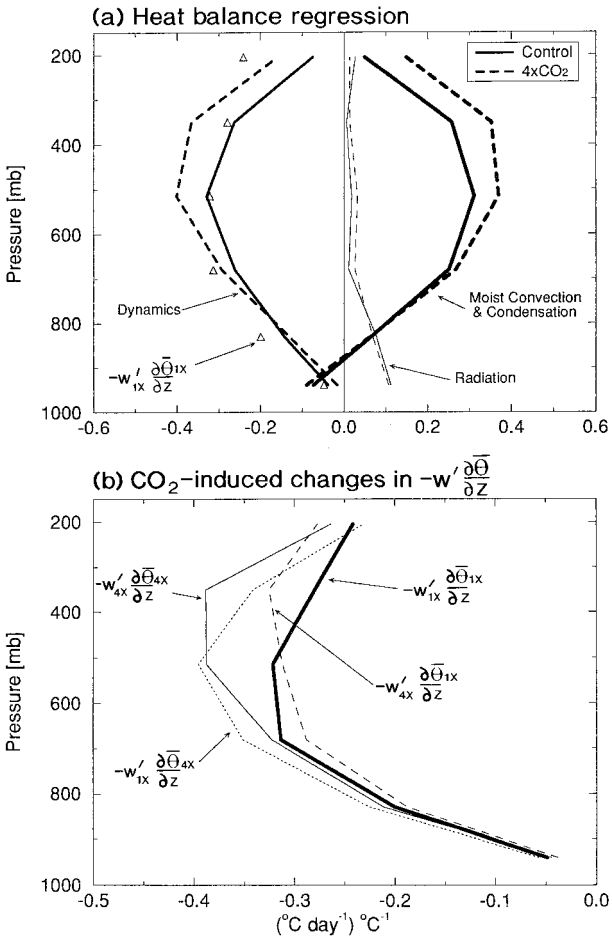

FIG. 14. Linear regression of model tropospheric heat balance components (averaged 11°N–11°S, 173°E–113°W) vs SST (averaged 7°N–7°S, 173°E–120°W). Results are for 0 lag based on 2–7-yr bandpass-filtered data for years 1–200 and 301–500 of the control and 4 × CO_2 experiments, respectively. The heat balance terms are based on a potential temperature form of the heat balance (see Knutson and Manabe 1995, appendix A, for details). Shown are profiles of (a) heating due to dynamics, radiation, and moist convection and condensation from the control (solid) and 4 × CO_2 (dashed) experiments, along with the simplified dynamical cooling expression $-w'\,\partial(\theta)/\partial z$ from the control experiment (triangles); and (b) diagnosis of CO_2-induced changes in the term $-w'\,\partial(\theta)/\partial z$ for various combinations of w' and $\partial\theta/\partial z$ from the control and 4 × CO_2 experiments (see text). Units are (°C day^{-1}) °C^{-1}.

vection and condensation is primarily balanced by dynamical cooling anomalies (Fig. 14a), with radiative heating anomalies playing a relatively minor role. Similarly, the CO_2-induced enhancement of condensation heating is roughly balanced by a CO_2-induced enhancement of dynamical cooling. These results are in contrast to the model's climatological mean tropospheric heat balance over the western tropical Pacific (discussed in Knutson and Manabe 1995) where radiative cooling was of comparable importance to dynamical cooling in balancing the condensation heating.

The total dynamical cooling anomaly can be roughly approximated by the term $-w' \partial(\overline{\theta})/\partial z$ (where w' is the vertical velocity anomaly and θ is the time-mean potential temperature) as shown by a comparison of the solid dynamical cooling curve and the triangles in Fig. 14a. Therefore, to simplify the analysis, CO_2-induced changes in just the term $-w' \partial(\overline{\theta})/\partial z$ are examined in Fig. 14b. By artificially combining the vertical motion anomaly field from either the control or $4 \times CO_2$ experiment with the time-mean potential temperature from the other experiment $4 \times CO_2$ or control, respectively) the relative effects of CO_2-induced changes in vertical velocity and static stability can be assessed. The effect of CO_2-induced changes in vertical velocities alone (comparing $-w'_{1x} \partial(\overline{\theta_{1x}})/\partial z$ with $-w'_{4x} \partial(\overline{\theta_{1x}})/\partial z$) is to enhance the dynamical cooling in the upper troposphere while slightly suppressing dynamical cooling in the middle and lower troposphere. The enhanced upper tropospheric cooling is due to slightly intensified vertical motion anomalies (per °C) in the upper troposphere in the $4 \times CO_2$ experiment, which results from the slightly deeper average penetration of convection anomalies in the warmer climate. The effect of CO_2-induced increases in the time-mean static stability, $\partial\overline{\theta}/\partial z$, is to enhance the dynamical cooling (for a given vertical motion anomaly) over a large layer of the middle troposphere (comparing $-w'_{1x}\partial(\overline{\vartheta_{1x}})/\partial z$ with $-w'_{1x} \partial(\overline{\theta_{4x}}/\partial z$. The enhancement of $-w' \partial(\theta/\partial z$ due to the increased time-mean static stability effect alone is equivalent to 75% of the total enhancement of the vertically integrated tropospheric dynamical cooling. The increased time-mean static stability is an effect of moist convection, which keeps the vertical lapse of temperature close to the moist adiabatic rate, making $\partial\theta/\partial z$ larger in a warmer atmosphere. Thus, the time-mean lapse rate mechanism helps us to interpret why the zonal overturning circulation anomalies, and hence surface zonal wind anomaly (per °C), does not increase in proportion to the increase of condensation heating (per °C) in the model.

In terms of the ocean component of the coupled model, the CO_2-induced decrease in the amplitude of the model ENSO's SST fluctuations is accompanied by changes in the mean state of the model's tropical Pacific Ocean. In the $4 \times CO_2$ experiment, the time-mean zonal SST contrast along the equator is reduced by about 20% (Knutson and Manabe 1995), the thermocline is more diffuse with a reduced east–west slope, and the ocean's equatorial surface currents are substantially weaker. These changes apparently reduce the potential energy in the mean state that ENSO can extract, leading to a reduction in the variability of SST. In addition to mean state changes, enhanced evaporative damping of SST anomalies occurs in the $4 \times CO_2$ climate, since the evaporation anomalies are larger (per °C SST anomaly) with the warmer basic state. Thus, increased evaporative damping acts to reduce ENSO variability through two mechanisms: first (directly) by stronger evaporative damping of the SST anomalies themselves, and second, (indirectly) by acting to reduce the time-mean zonal SST gradient (see Knutson and Manabe 1995). This preliminary assessment of the mechanisms for the reduced SST variability in the model is based on analyses of the ocean surface layer heat budget. However, more definitive statements about the mechanisms of the model response cannot be made based on a surface layer heat balance analysis alone, since such an analysis does not include the role of the subsurface dynamics, which is an important component of the model ENSO.

6. Summary and concluding remarks

In this report, an analysis has been presented of simulated ENSO phenomena occurring in three 1000-yr simulations using the GFDL low-resolution (R15) global coupled ocean–atmosphere general circulation model (GCM). In the control simulation, the model ENSO's SST fluctuations are too small in amplitude, particularly in the eastern equatorial Pacific, compared with observations or with higher-resolution model simulations. Nevertheless, the life cycle of the model ENSO is qualitatively similar in many respects to the delayed-oscillator life cycle simulated in higher resolution models. This indicates that the essential physical mechanism of ENSO is simulated in the coupled model despite the coarse resolution.

Wavelet analyses of an 820-yr record of model SSTs and a multicentury paleo-SST record inferred from coral $\delta^{18}O$ measurements (Dunbar et al. 1994) reveal that on interannual (2–7 yr) timescales, substantial multidecadal amplitude modulation occurs in both the model and paleo-SST records. This amplitude modulation is broadly consistent with the secular changes in ENSO amplitude documented from instrumental SST records from the past century. A two-dimensional wavelet analysis indicates that the preferred frequency of spectral ''peaks'' also varies with time for both the model SST and $\delta^{18}O$ data. The model results suggest that variations in ENSO's amplitude and frequency reported in previous observational studies could be due in large part to internally generated variability of the coupled ocean–atmosphere system.

The recent prolonged (1990–1995) warm event in the

tropical Pacific has raised new questions about our understanding of the climate variability in that region. Trenberth and Hoar (1996) suggest that the event is unlikely to be a natural decadal-scale variation, but may be partly caused by increased greenhouse gases. On the other hand, our 2D wavelet results in Fig. 7 clearly indicate that on decadal (8–15 yr) timescales, pronounced variability appears sporadically or intermittently in the model (Fig. 7b), and perhaps also in the real world (coral data results in Fig. 7a). Therefore, on the basis of currently available data, we would not eliminate the possibility of a sporadic appearance of substantial decadal-scale variability in the tropical Pacific region. Such variability, if present, would complicate detection of greenhouse gas-induced warming in the region.

Concerning the model's multidecadal amplitude modulation, we have not yet determined the underlying physical mechanism for this phenomenon. We have speculated that a number of mechanisms may be at least partly responsible for producing the modulation behavior. Among the possibilities considered were (i) multidecadal fluctuations in the model's basic state, which in turn affect the model ENSO's amplitude; (ii) irregular behavior resulting from low-order chaos; and (iii) irregular behavior resulting from the stochastic forcing of a dynamical system. Regarding mechanism (i), no evidence has yet been found for multidecadal mean state fluctuations that are highly correlated with the amplitude modulation series. For example, global SST, tropical Pacific SST gradients, the east–west slope of the thermocline, surface salinity, etc. have been examined. However, the CO_2 sensitivity experiments indicate that some characteristics of the amplitude modulation, such as its relative size and timescale, are affected by CO_2-induced global warming. Concerning mechanism (ii), it is clear that a pronounced amplitude modulation occurs in the Cane–Zebiak model (e.g., Fig. 8e), whereas, according to Tziperman et al. (1994), time series from the Cane–Zebiak model are consistent with a low-order chaos mechanism. However, Chang et al. (1996) suggest that the simulated ENSO in our coupled model is not driven by low-order chaos, but rather results from stable dynamics driven by higher-frequency stochastic atmospheric processes, which leads us to speculate that mechanism (iii) may be important for our model's amplitude modulation. Nonetheless, at this stage we cannot conclude which, if any, of the above potential mechanisms are important to the model's amplitude modulation.

The sensitivity of the model's ENSO to increased CO_2 was examined using three 1000-yr experiments (Control, $2 \times CO_2$, and $4 \times CO_2$), with CO_2 increasing by a factor of two (four) during the first 70 (140) yr of the latter two experiments. Despite the $\sim$5°C warming of the tropical Pacific, and $\sim$50% increase in time-mean atmospheric water vapor under $4 \times CO_2$ conditions, ENSO-related SST fluctuations in the coupled model do not intensify, but rather decrease slightly in amplitude. Roughly a 20% decrease occurs in the standard deviation of tropical Pacific SST fluctuations (7°N–7°S, 173°E–120°W) for both the $2 \times CO_2$ and $4 \times CO_2$ experiments in comparison to the control experiment. This slight CO_2-induced reduction of SST variability does not appear to be sensitive to the particular frequency band considered (2–7 yr, 8–15 yr, 2–15 yr, etc.). The decreased SST variability appears to be due to several factors, including CO_2-induced changes in the model's basic state. For example, Knutson and Manabe (1995) noted a 20% reduction in the time-mean zonal SST gradient due to enhanced evaporative damping in the $4 \times CO_2$ climate. The *peak* ENSO-related precipitation anomalies (per °C SST anomaly) are enhanced by about 50% and are shifted slightly eastward in the $4 \times CO_2$ experiment, relative to the control. The *large-scale* precipitation anomaly over the central Pacific (per °C) is enhanced by about 24% in the $4 \times CO_2$ case relative to the control, but since the SST variability *decreases,* the net change in large-scale precipitation variability in the region is comparatively small. The substantial CO_2-induced enhancement of precipitation anomalies (per °C) is accompanied by a much smaller percentage change in the surface wind anomalies (per °C). This result can be interpreted in terms of the model's tropospheric heat balance. In the heat balance, the CO_2-induced enhancement of condensation heating anomalies is offset by enhanced dynamical cooling, with the latter resulting in large part from increased time-mean static stability in the warmer climate, rather than circulation changes. In contrast to the weaker overall amplitude of SST fluctuations, the multi-decadal amplitude *modulations* become more pronounced with increased CO_2. The *frequency* of simulated ENSO events in the model does not appear to be markedly changed by increased CO_2.

Although the low-resolution R15 coupled model appears to capture the essential physical mechanism of ENSO, it will be important to repeat these experiments using higher resolution coupled models to examine the possible impact of increasing model resolution on our conclusions. It will also be desirable to repeat the experiments with a model that does not require flux adjustments to reduce climate drift, once such models become available. As a preliminary step toward higher resolution, two much shorter (80 year) experiments using a global coupled model (including flux adjustment) with twice the horizontal resolution (i.e., R30) and approximately twice the vertical resolution of our R15 coupled model have been examined. The two R30 experiments include a control run with constant CO_2 and a perturbation run with CO_2 increasing at 1% per year (compounded). The amplitude of interannual SST variability in the R30 model is more realistic than in the R15 model, with fluctuations of up to 3°C. A shortcoming of the R30 model is that the peak interannual SST variability is located

even further to the west (i.e., near the date line) than in the R15 experiment. In the R30 CO_2-perturbation experiment, no pronounced long-term trends are evident in either the amplitude or other characteristics of the model's interannual SST variability. Nonetheless, only a very large CO_2–ENSO sensitivity can be ruled out for the R30 coupled model at present, owing to the short length of integration (80 years) available for analysis thus far.

The substantial multidecadal modulation of ENSO's amplitude during the past century appears to have been typical of ENSO's behavior over the past several centuries. If a large portion of this amplitude modulation is internally generated in the climate system—as is suggested by results from a control run of our R15 coupled model—then the detection and attribution of anthropogenic (or other external) influences on ENSO is likely to be very difficult, owing to the presence of this large ''noise'' component in the system. An important finding of this study is that even using a time horizon of several decades, the internally generated amplitude modulation can obscure the change in amplitude induced by increasing CO_2 in the model. One cannot rule out the possibility that the sensitivity of ENSO to increased CO_2 is substantially larger (or smaller) than that estimated with the R15 coupled model, in which case it would be much easier (or harder) to detect a CO_2-induced change in its character. However, if the model ENSO's CO_2 sensitivity and internal variability are even approximately correct, the implication is that a CO_2-induced impact on ENSO is not likely to become clearly evident for many decades, and possibly centuries.

Acknowledgments. We thank J. Anderson, I. Held, T. Schneider, an anonymous reviewer, and others for helpful comments; R. Stouffer for providing the results from the successful long-term integrations of the R15 coupled model; R. Dunbar for making the coral data publicly available; S. Zebiak for providing the Cane–Zebiak model output; M. Spelman and K. Dixon for conducting the R30 coupled experiments; and B. Doty and P. Turner for providing graphics software.

REFERENCES

Battisti, D. B., and A. C. Hirst, 1989: Interannual variability in a tropical atmosphere–ocean model: Influence of the basic state, ocean geometry, and nonlinearity. *J. Atmos. Sci.,* **46,** 1687–1712.

Chang, P., L. Ji, H. Li, and M. Flügel, 1996: Chaotic dynamics versus stochastic process in El Niño–Southern Oscillation in coupled ocean–atmosphere models. *Physica D,* in press.

Chao, Y., and S. G. H. Philander, 1993: On the structure of the Southern Oscillation. *J. Climate,* **6,** 450–469.

Chatfield, C., 1975: *The Analysis of Time Series: Theory and Practice.* Chapman and Hall, 263 pp.

Combes, J. M., A. Grossmann, and P. Tchamitchian, Eds., 1989: *Wavelets: Time-Frequency Methods and Phase Space.* Springer-Verlag, 315 pp.

Diaz, H. F., and V. Markgraf, 1992: *El Niño: Historical and Paleoclimatic Aspects of the Southern Oscillation.* Cambridge University Press, 476 pp.

——, and R. S. Pulwarty, 1994: An analysis of the time scales of variability in centuries-long ENSO-sensitive records in the last 1000 years. *Climate Change,* **26,** 317–342.

Dunbar, R. B., G. M. Wellington, M. W. Colgan, and P. W. Glynn, 1994: Eastern Pacific sea surface temperature since 1600 A.D.: The δ^{18}O record of climate variability in Galápagos corals. *Paleoceanogr.,* **9,** 291–315.

Enfield, D. B., and L. Cid S., 1991: Low-frequency changes in El Niño–Southern Oscillation. *J. Climate,* **4,** 1137–1146.

Farge, M., 1992: Wavelet transforms and their applications to turbulence. *Annu. Rev. Fluid Mech.,* **24,** 395–457.

Goddard, L., 1995: The energetics of interannual variability in the tropical Pacific Ocean. Ph. D. dissertation, Princeton University, 210 pp.

Graham, N. E., and W. B. White, 1988: The El Niño cycle: A natural oscillator of the Pacific ocean–atmosphere system. *Science,* **240,** 1293–1302.

Gu, D., and S. G. H. Philander, 1995: Secular changes of annual and interannual variability in the Tropics during the past century. *J. Climate,* **8,** 864–876.

Hamming, R. W., 1977: *Digital Filters.* Prentice-Hall, 226 pp.

Honerkamp, J., 1994: *Stochastic Dynamical Systems: Concepts, Numerical Methods, Data Analysis.* VCH Publishers, 535 pp.

Jin, F.-F., and J. D. Neelin, 1993: Modes of interannual tropical ocean–atmosphere interaction—A unified view. Part I: Numerical results. *J. Atmos. Sci.,* **50,** 3477–3503.

Julian, P. R., 1975: Comments on the determination of significance levels of the coherence statistic. *J. Atmos. Sci.,* **32,** 836–837.

Knutson, T. R., and S. Manabe, 1994: Impact of increased CO_2 on simulated ENSO-like phenomena. *Geophys. Res. Lett.,* **21,** 2295–2298.

—— and ——, 1995: Time-mean response over the tropical Pacific to increased CO_2 in a coupled ocean–atmosphere model. *J. Climate,* **8,** 2181–2199.

Lau, N.-C., S. G. H. Philander, and M. J. Nath, 1992: Simulation of ENSO-like phenomena with a low-resolution coupled GCM of the global ocean and atmosphere. *J. Climate,* **5,** 284–307.

Manabe, S., and R. J. Stouffer, 1994: Multiple century response of a coupled ocean–atmosphere model to an increase of atmospheric carbon dioxide. *J. Climate,* **7,** 5–28.

——, ——, M. J. Spelman, and K. Bryan, 1991: Transient response of a coupled ocean–atmosphere model to gradual changes of atmospheric CO_2. Part I: Annual mean response. *J. Climate,* **4,** 785–818.

Meehl, G. A., 1990: Seasonal cycle forcing of El Niño–Southern Oscillation in a global, coupled ocean–atmosphere model. *J. Climate,* **3,** 72–98.

——, G. W. Branstator, and W. M. Washington, 1993: Tropical Pacific interannual variability and CO_2 climate change. *J. Climate,* **6,** 42–63.

Michaelsen, J., 1989: Long-period fluctuations in El Niño amplitude and frequency reconstructed from tree rings. *Aspects of Climate Variability in the Pacific and the Western Americas. Geophys. Monogr.,* No. **55,** Amer. Geophys. Union, 69–74.

Neelin, J. D., 1991: The slow sea surface temperature mode and the fast-wave limit: Analytic theory for tropical interannual oscillations and experiments in a hybid coupled model. *J. Atmos. Sci.,* **48,** 584–606.

——, and Coauthors, 1992: Tropical air–sea interaction in general circulation models. *Climate Dyn.,* **7,** 73–104.

Pan, Y. H., and A. H. Oort, 1990: Correlation analyses between sea surface temperature anomalies in the eastern equatorial Pacific and the World Ocean. *Climate Dyn.,* **4,** 191–205.

Philander, S. G. H., R. C. Pacanowski, N.-C. Lau, and M. J. Nath, 1992: Simulation of ENSO with a global atmospheric GCM coupled to a high-resolution, tropical Pacific Ocean GCM. *J. Climate,* **5,** 308–329.

Rasmusson, E. M., and T. H. Carpenter, 1982: Variations in tropical sea surface temperature and surface wind fields associated with the Southern Oscillation/El Niño. *Mon. Wea. Rev.,* **110,** 354–384.

Ropelewski, C. F., and M. S. Halpert, 1987: Global and regional scale precipitation patterns associated with the El Niño/Southern Oscillation. *Mon. Wea. Rev.,* **115,** 1606–1626.

Schopf, P. S., and M. J. Suarez, 1988: Vacillations in a coupled ocean–atmosphere model. *J. Atmos. Sci.,* **45,** 549–566.

Tett, S., 1995: Simulation of El Niño–Southern Oscillation-like variability in a global AOGCM and its response to CO_2 increase. *J. Climate,* **8,** 1473–1502.

Trenberth, K. E., 1976: Spatial and temporal variations of the Southern Oscillation. *Quart. J. Roy. Meteor. Soc.,* **102,** 639–653.

——, and D. J. Shea, 1987: On the evolution of the Southern Oscillation. *Mon. Wea. Rev.,* **115,** 3078–3096.

——, and T. J. Hoar, 1996: The 1990–1995 El Niño–Southern Oscillation Event: Longest on record. *Geophys. Res. Lett.* **23,** 57–60.

Tziperman, E., L. Stone, M. A. Cane, and H. Jarosh, 1994: El Niño chaos: Overlapping of resonances between the seasonal cycle and the Pacific ocean–atmosphere oscillator. *Science,* **264,** 72–74.

Wang, X. L., and C. F. Ropelewski, 1995: An assessment of ENSO-scale secular variability. *J. Climate,* **8,** 1584–1599.

Wilks, D. S., 1995: *Statistical Methods in the Atmospheric Sciences.* Academic Press, 467 pp.

Zebiak, S. E., and M. A. Cane, 1987: A model El Niño–Southern Oscillation. *Mon. Wea. Rev.,* **115,** 2262–2278.

——, and ——, 1991: Natural climate variability in a coupled model. *Greenhouse Gas-Induced Climatic Change: A Critical Appraisal of Simulations and Observations.* M. E. Schlesinger, Ed., Elsevier, 457–469.